Master's Thesis

F4

Faculty of Nuclear Sciences and Physical Engineering
Department of Physics

Application of Semiconductor Detectors in Fusion Experiments

Bc. Peter Švihra

Supervisor: Ing. Michal Marčišovský, PhD.
Field of study: Physics and Technology of Thermonuclear Fusion
May 2018

Diplomová práce

F4

Fakulta jaderná a fyzikálně inženýrská
Katedra Fyziky

Použití polovodičových detektorů ve fúzních experimentech

Bc. Peter Švihra

Školitel: Ing. Michal Marčišovský, PhD.
Obor: Fyzika a technika termojaderné fúze
Květen 2018

ČESKÉ VYSOKÉ UČENÍ TECHNICKÉ V PRAZE
FAKULTA JADERNÁ A FYZIKÁLNĚ INŽENÝRSKÁ
PRAHA 1 - STARÉ MĚSTO, BŘEHOVÁ 7 - PSČ 115 19

Katedra: fyziky *Akademický rok:* 2017/18

ZADÁNÍ DIPLOMOVÉ PRÁCE

Student: Bc. Peter Švihra

Studijní program: Aplikace přírodních věd

Obor: Fyzika a Technika Termojaderné Fúze

Název práce: (česky) Použití polovodičových detektorů ve fúzních experimentech

Název práce: (anglicky) Application of Semiconductor Detectors in Fusion Experiments

Pokyny pro vypracování:

1. Ubíhající elektrony v tokamacích
2. Polovodičové křemíkové detektory ionizujícího záření
3. Simulace interakce ionizujícího záření se součástmi tokamaku
4. Měření a analýza dat na tokamaku COMPASS

Práce bude vypracována v anglickém jazyce.

Doporučená literatura:

1. P. Kulhánek: Úvod do teorie plazmatu, AGA, 2011
2. J. Wesson: TOKAMAKS, Oxford University Press, 2011
3. G. F. Knoll: Radiation Detection and Measurement, Wiley, 2010
4. G. Lutz: Semiconductor Radiation Detectors, Springer, 1999

Jméno a pracoviště vedoucího diplomové práce:

Ing. Michal Marčišovský, PhD., Katedra fyziky, Fakulta jaderná a fyzikálně inženýrská ČVUT v Praze

Datum zadání diplomové práce: 20.10.2017

Termín odevzdání diplomové práce: 07.05.2018

Doba platnosti zadání je dva roky od data zadání.

…….. ……..
vedoucí katedry *děkan*

V Praze dne 20.10.2017

Acknowledgements

I want to express my sincere gratitude to my supervisor Ing. Michal Marčišovský, PhD., for his time, advice and support throughout my studies. He helped me to bring out the best in myself and taught me the difficult and subtle ways of science.

My thanks also belong to my colleague, Ing. Mária Marčišovská, for language revisions. Additionally, I would like to thank all my colleagues for assistance with measurements, development of readout modules and for being wonderful companions. This recognition also belongs to the head of our group, Dr. Václav Vrba, for all the help and opportunities he provided.

Next, I would like to thank the teams from both tokamak GOLEM and tokamak COMPASS for providing access and information about the experiments, as well as needed feedback on my work.

Since art of my work was performed using devices from the Medipix family, I want to express my gratitude to the whole Medipix collaboration, especially to the team from Nikhef institute, and Dr. Andrei Nomerotski from Brookhaven National Laboratory for their vast knowledge and insight into semiconductor detectors.

Last but not least, I would like to thank my whole family and my partner Lucie, as I would not have finished this work without their support and encouragement.

Declaration

I hereby declare, that I have written this thesis by myself and I have used only the materials stated in the references section.

I have no reason to object to use this work according to the section 60 of Act No. 121/2000 Coll.,On Copyright, on Rights Related to Copyright, and on Change of Some Acts (Copyright Act)

Prague, May 7, 2018

Abstract

Discharges in the experimental devices tend to undergo a rapid termination – disruption. In tokamaks, plasma disruption can result in emergence of relativistic electron population accelerated to MeV-order energies. These so-called runaway electrons (RE) then behave like in a particle accelerator and can cause damage to the vacuum vessel and other critical components.

Since the disruptions tend to generate detectable primary and secondary radiation, new diagnostic methods, such as proposed semiconductor pixel detectors, are viable and innovative addition to existing diagnostic systems. In order to successfully operate such detectors, different instrumental calibration processes have been developed and performed. As a result, relevant information about the spatial and temporal distribution of RE has been acquired. This is crucial for further advancements of the fusion research and understanding of the RE generation process.

Results of the measurements from different experiments are promising, however, their non-trivial interpretation requires further analysis and simulations of the experiment. For this purpose a Geant4 toolkit has been utilized, modeling transportation and interaction of RE and their secondary particles in tokamak COMPASS. Implementation of such model could be further exploited for radiation and device operational safety.

Keywords: tokamak, runaway electrons, semiconductor detectors, Medipix, Geant4

Title: Application of Semiconductor Detectors in Fusion Experiments

Supervisor: Ing. Michal Marčišovský, PhD.

Abstrakt

Výboje plazmatu v experimentálních zařízeních procházejí často procesem rychlé terminace neboli disrupce. V tokamaku mohou disrupce plazmatu vyvolat vznik populace vysokoenergetických elektronů, tzv. ubíhající elektrony – runaway electrons (RE), které jsou dále urychlovány obdobně jako v urychlovačích částic a mohou způsobit značné škody na vakuové komoře nebo na jiných důležitých komponentech.

Jelikož disrupce generují detekovatelné primární a sekundární záření, nové diagnostické metody, například využití navrhovaných polovodičových pixelových detektorů, jsou inovativním doplněním existujících diagnostických systémů. Před zahájením detekce záření je potřeba provést důkladné kalibrace zařízení, které slouží k přesnější interpretaci prostorové a časové distribuce RE. Závěry z měření mohou vést ke značným pokrokům v porozumění procesů týkajících se generace RE.

Správná interpretace dat získaných z různých experimentů není triviální, proto bylo potřeba naměřená data dále analyzovat a vytvořit simulace pro jednotlivé experimenty. Součástí diplomové práce bylo vytvoření modelu transportu a interakce RE pomocí simulačního nástroje Geant4. Vytvořený model by mohl poskytnout spolehlivý prostředek pro účely zajištění bezpečnosti na pracovišti i ochranu samotného zařízení.

Klíčová slova: tokamak, ubíhající elektrony, polovodičové detektory, Medipix, Geant4

Název: Použití polovodičových detektorů ve fúzních experimentech

Školitel: Ing. Michal Marčišovský, PhD.

Contents

Figures

Chapter 1

Introduction

Thermonuclear fusion is considered a perspective future energy source. The development started in the second half of the 20th century as a way of peacefully harnessing the power accessible only by the stars and fusion bombs. Many different devices were constructed, hoping to produce more energy than was consumed for operation. This ranged from small tabletop-sized experiments up to large ones currently being tested or developed.

One of the first types of devices unleashing the fusion energy were pinches, simple wires which are heated and compressed by large electric currents flowing through them and subsequently created magnetic field. This configuration works in pulses only and is a subject to emergence of different magnetohydrodynamic plasma instabilities. After a long research period, it was shown that even with scaling to the larger sizes, the device is not capable of generating large fusion yield. However, it proved to be a suitable device for study of instabilities, development of many diagnostics techniques and it is widely used as a laboratory X-ray or neutron source.

On the other hand, tokamaks (from Russian "toroidal'naya kamera s magnitnymi katushkami" – toroidal chamber with magnetic coils) are devices more complex in magnitude to construct, showing promising results for technology of an operational fusion reactor. They are using electromagnetic induction, microwaves, accelerated neutral atoms or their combination to heat and ionize gas. The confinement is provided by a magnetic field, generated by the coils around the toroidally-shaped chamber, together with the field created by induced electric current in plasma. By this process, particles receive necessary kinetic energy to overcome Coulomb barrier and undertake thermonuclear fusion – typically a deuterium-tritium reaction, which produces energy, helium atom and a neutron. For a typical tokamak plasma density, the confinement time falls within the range of a few seconds and can be terminated by disruptions.

One of the possible outcomes of a disruption is generation of electrons with high energy – so called Runaway Electrons (RE). Their generation at large tokamaks can cause damage to the vacuum vessel, as is shown in figure 1.1.

Since the RE generation process is still not well understood, new diagnostic methods are necessary, providing information about time and position of impact of an electron beam. Semiconductor detectors are widely used in High

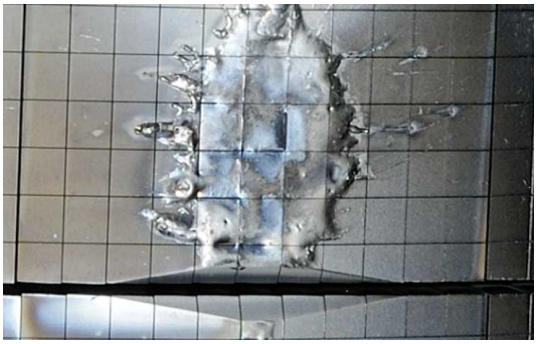

Figure 1.1: Re-deposited molten beryllium appears on tiles inside the JET vessel after experiments focused on RE generation and effects.[1]

Energy Physics (HEP) as particle tracking detectors – due to their sensitivity to ionizing radiation. They can also be successfully applied in new system for plasma diagnostic applications.

In the second chapter, a short introduction to tokamak devices is made. Comparison of limiter and divertor configuration is discussed with a follow-up on differences between opperation modes. Lastly a short description of two Czech tokamaks, GOLEM and COMPASS, is made.

The third chapter is focused on different types of instabilities that occur in tokamaks, mostly the ones with highest risk to the operation of large devices. RE processes are thoroughly described with different ways of RE generation.

Introduction to the semiconductor detector physics is made in the fourth chapter. At first, interactions of ionizing radiation with matter are described – relevant for both processes of RE interaction and electron-hole production in the semiconductor detectors. The chapter follows up with short description of p-n junction and signal generation, visualized on simulations from a Weightfield2 toolkit developed by European Organization for Nuclear Research (CERN). Lastly, different detectors and readouts are characterized, discussing techniques of enhancing the detector response.

The fifth chapter interlinks the physics of tokamaks and semiconductor detectors via Monte Carlo simulations. Short introduction to Geant4 simulation toolkit is made, followed up by its implementation. The simulations are focused on the interaction of ionizing radiation with matter, their main objective is to develop a 3D model of tokamak COMPASS in order to monitor interactions of RE and subsequent secondary particles.

In the last chapter, number of measurements at both tokamkas GOLEM and COMPASS is described. The results show promising application of semiconductor pixel detectors due to their exceptional temporal and spatial resolution. Moreover, RE radiation profiles from Geant4 simulation of tokamak COMPASS describe the angular dependency and detector response.

Thesis is summarized in the conclusions chapter, discussing the results from both measurements and simulations. Furthermore, suggestions for the advancement and application of the work are provided.

Chapter 2

Tokamaks

The simplest criterion of achieving positive yield in thermonuclear fusion (producing more energy than was consumed) was derived by Lawson [2] in a form:

$$n_{\mathrm{p}}\tau = \frac{12 k_{\mathrm{B}} T}{\langle \sigma v \rangle E_{\mathrm{f}}}, \tag{2.1}$$

where n_{p} is the density of plasma, τ is containment time, k_{B} is Boltzmann constant, E_{f} is the total energy output, and $\langle \sigma v \rangle$ is reaction rate (dependent on T). For D-T fusion, the Lawson's criterion is $n_{\mathrm{p}}\tau \geq 1 \cdot 10^{14}\,\mathrm{s\,cm^{-3}}$.

It is easily derived from the formula above, for a large confinement time τ, plasma density n_{p} can be smaller and vice-versa. These boundary values can be achieved in magnetic ($n_{\mathrm{p}} \sim 1 \cdot 10^{14}\,\mathrm{cm^{-3}},\ \tau \sim 1\,\mathrm{s}$), or inertial confinement ($n_{\mathrm{p}} \sim 1 \cdot 10^{23}\,\mathrm{cm^{-3}},\ \tau \sim 1 \cdot 10^{-9}\,\mathrm{s}$). Fusion experiments with low plasma density such as tokamaks, spheromaks and stellarators belong to the magnetic confinement category, whereas laser driven fusion is a type of the inertial confinement.

2.1 Basic information

Standard tokamak configuration is a toroidal vacuum vessel, possibly in a more advanced D-shaped geometry. The vessel is surrounded by toroidal and poloidal magnets, providing field for confinement of plasma. This simplified geometry is shown in figure 2.1. Moreover, different tools for fusion diagnostics and heating are positioned all around the torus.

Currently, the largest experiment, called ITER, (from Latin *iter* – direction, way) is being built in Cadarache, France. There are around 200 tokamaks around the world, two of them in Prague, Czechia – the oldest operational tokamak GOLEM (previously CASTOR) and medium-sized tokamak COMPASS.

2.2 Description of tokamak

Due to the tokamak device symmetry, a toroidal coordinate system is used with toroidal direction φ (following the torus), poloidal direction θ (perpendicular

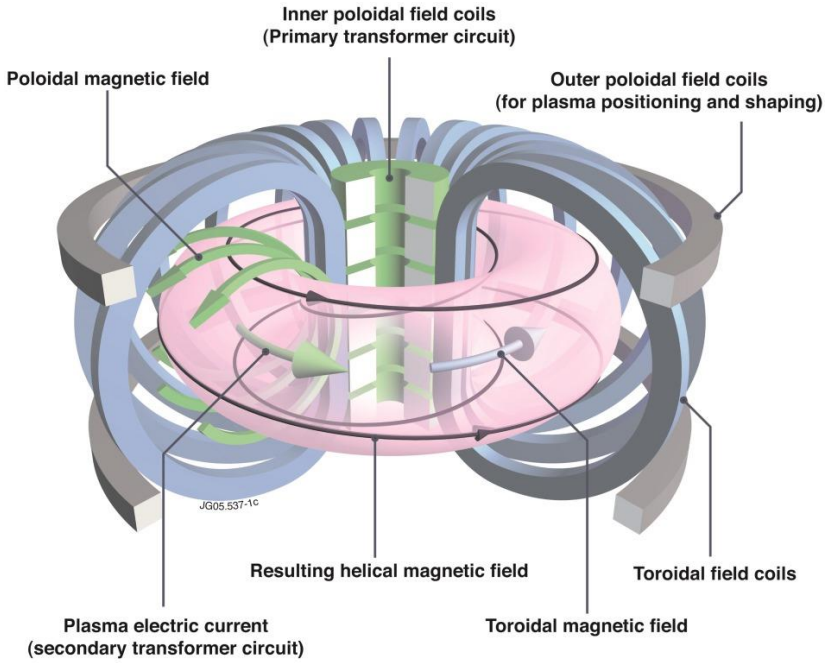

Figure 2.1: Schematic of a tokamak device, basic process of plasma containment using combination of toroidal and poloidal magnetic field. [3]

to toroidal) and radial direction r. For a better description of torus two radii are used: major radius R_0, describing size of the torus from the middle to the centre of the vessel (so called magnetic axis), and minor radius a, describing distance from the magnetic axis to the rim of the torus.

The coils usually generate a toroidal field with a magnetic induction of the order of 1 T. One of the important parameters is β, which compares plasma thermal pressure p_p to the pressure of magnetic field B, following equation

$$\beta = \frac{p_\mathrm{p}}{B^2/2\mu_0}. \tag{2.2}$$

In tokamaks B^2 contains combination of both toroidal and poloidal fields.

To achieve the emergence of helical magnetic field and ohmic heating of the plasma, a current I_p is induced in plasma. For that purpose, a primary winding of a transformer in the middle of the tokamak is needed with plasma being the secondary winding. The downside of such method is that the current in the primary winding must be increasing and that is impossible for long device operation. Moreover, the resistance of plasma is decreasing with higher temperatures making ohmic heating inapplicable, therefore methods of additional heating have been developed. The most widely used are neutral beam injection and heating via electromagnetic waves at electron and ion cyclotron frequencies.

The combined helical magnetic field consists of toroidal field from coils and poloidal magnetic field created by induced current according to Ampère's law. The fraction of poloidal to toroidal field is best described by the safety

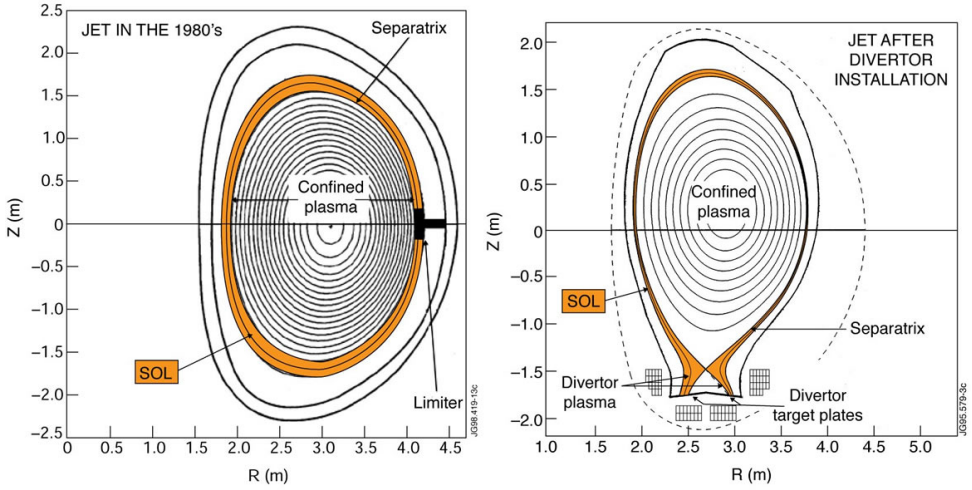

Figure 2.2: Comparison of limiter and divertor configuration of tokamak. Separatrix (last closed flux surface) and scrape-off layer (SOL) are highlighted. [1].

factor q. It compares the number of rotations of magnetic field lines needed in toroidal direction, to achieve one rotation in poloidal direction. Typically tokamaks operate at $q \approx 3$ at the outer side of the field, since larger values tend to lead to instabilities. [3] The ideal safety factor would be imaginary, implying that the field lines would never connect.

Plasma confined in the torus tends to drift, therefore additional poloidal coils are used to help shape the plasma (see fig. 2.1). Different diagnostic systems are used for feedback, enabling real-time calculation of needed generated field to help contain the plasma.

Historically, the shape of the vessel was circular at first, however, it was later modified to a D-shape. This was due to plasma having more particles in a stronger magnetic field, since the intensity of the magnetic field decreases as $1/r$, the middle of the torus represents so called High Field Side (HFS) and the outer part is Low Field Side (LFS). Such plasma configurations are called elongated, instead of circular. Another reason for the D-shaped configuration of tokamak was due to the better stability and construction of the device – toroidal coils constructed this way are mechanically sturdier.

Another main concern in tokamak devices is interaction of hot plasma with the walls of the vacuum vessel. By interacting, the vessel material can enter the plasma and contaminate it, causing radiative energy losses (scaling as square of atomic number Z) and worsening plasma parameters. The last surface with enclosed magnetic field lines is called Last Closed Flux Surface (LCSF), or sparatrix, outside of which is Scrape-Off Layer (SOL). These surfaces are visualized in figure 2.2. Studies of SOL are important due to the interactions of plasma and disruptions with wall.

Former devices used a simple construction with limiter (obstacle limiting the plasma radius), later changed to the divertor construction (plasma primarily interacting with wall in a predefined region, usually at the bottom part of the

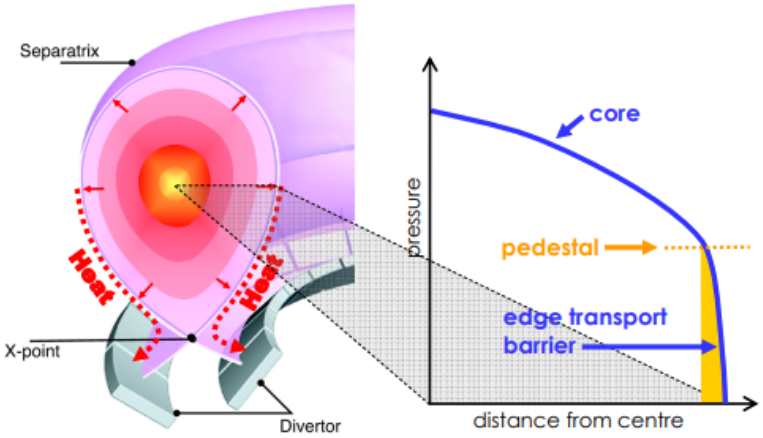

Figure 2.3: Schematic view of a divertor tokamak and pressure profile of its plasma. Pedestal and transport barrier is highlighted. [4].

torus). The divertor configuration includes X-point – point where $B_\theta = 0$. Using such construction of a tokamak lead to the discovery of H-mode, a regime with better plasma characteristics. It is caused by creation of a transport barrier which leads to a pedestal – region with higher values of parameters such as pedestal pressure p_{ped} or temperature T_{ped} (fig 2.3).

Different configuration types are compared in figure 2.2.

2.3 GOLEM

The tokamak GOLEM is an education-oriented tokamak located at the Faculty of Nuclear Sciences and Physical Engineering (FNSPE) at Czech Technical University (CTU) in Prague. It was formerly tokamak CASTOR, located at Institute of Plasma Physics (IPP) of the Czech Academy of Sciences (ASCR) in Prague.

Its major radius is $R_0 = 0.4\,\mathrm{m}$ and minor radius $a = 0.1\,\mathrm{m}$. The typical toroidal field is $B_{\mathrm{T}} \approx 0.4\,\mathrm{T}$ and plasma current in the flat-top phase $I_{\mathrm{p}} \approx 5\,\mathrm{kA}$. The usual pulse length is $t \approx 20\,\mathrm{ms}$.

Energy is stored in the capacitor banks, charged prior to each discharge.

A unique features of this experiment are the possibility of a complete remote handling operation via a secure Internet access and a firing rate roughly 1 discharge per 2 minutes.

2.4 COMPASS

The COMPASS tokamak of the IPP ASCR in Prague, is a medium-size experimental fusion device with ITER-like plasma cross-section, major radius $R_0 = 0.56\,\mathrm{m}$ and minor radius $a = 0.23\,\mathrm{m}$. The typical toroidal field is $B_{\mathrm{T}} = 1.2\,\mathrm{T}$ and plasma current in the flat-top phase $I_{\mathrm{p}} > 100\,\mathrm{kA}$. The usual pulse length is of the order of hundreds of ms.

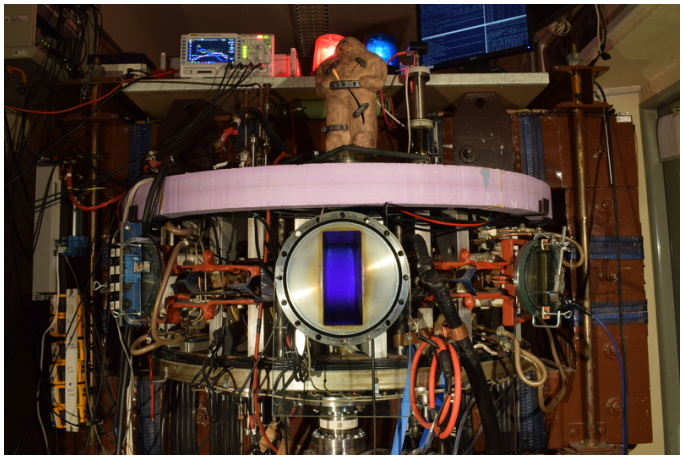

Figure 2.4: Image of tokamak GOLEM at FNSPE CTU.[1]

Since COMPASS is larger than GOLEM, energy for the magnetic systems and plasma heating is stored in a flywheel generator with total available power 45 MJs. Four AC/DC thyristors are then used as an interlink between the generator and tokamak. [5] The vacuum is pumped down to the range of $1.0 \cdot 10^{-6}$ Pa to $3.0 \cdot 10^{-6}$ Pa and the device operates with deuterium gas. The tokamak control system manages gas level during the discharge, enabling changes of plasma pressure and even injecting different types of gas during the discharge, such as argon. Before each operation, a glow discharge is used to clean the inner surface of the vacuum chamber of adsorbed particles.

The COMPASS plasma can be operated in both limiter and divertor configuration, the latter allowing H-mode operation.[6] Therefore, the tokamak can be operated similarly to ITER, which makes it very relevant for current fusion research.

The scientific experimental program of the tokamak is mainly focused on plasma edge physics, runaway electrons, and development of new diagnostic methods.

[1] `http://golem.fjfi.cvut.cz/?article=Chronicle/news` September: New photo of the GOLEM tokamak with plasma, by Dr. Vojtech Svoboda.

[2] `http://www.ipp.cas.cz/vedecka_struktura_ufp/tokamak/tokamak_compass/`, by IPP ASCR.

Figure 2.5: Image of tokamak COMPASS at IPP ASCR. [2]

Chapter 3

Plasma Disruptions

Due to the intrinsic properties of plasma, disruptions caused by hydrodynamic instabilities or by particle collisions exist. These natural processes are unwanted, observed in all experimental devices – causing difficulties related to the plasma confinement and even the device integrity.

Some of the most critical instabilities for the structural integrity of tokamak are presented in figure 3.1. They are further described, with a focus on RE.

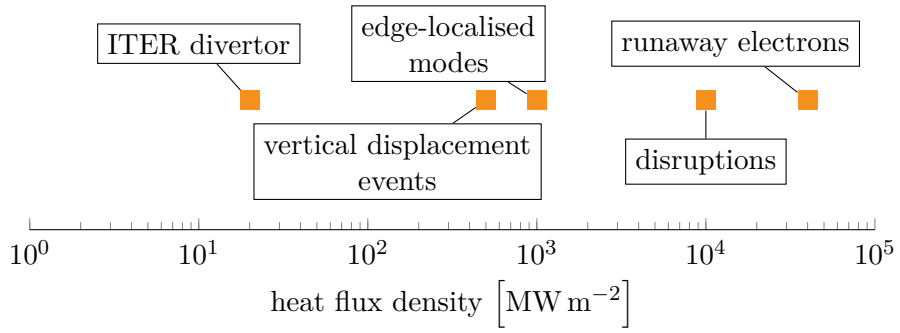

Figure 3.1: Heat flux density of different tokamak-related instabilities and maximal flux density at ITER divertor. Approximate plot made according to [7] and [8].

The greatest threat to the structural integrity of the vacuum vessel is from RE as is visible from the preceding figure.

3.1 Vertical Displacement Event

This event usually occurs for elongated plasmas, causing transport of whole plasma volume in vertical direction, eventually hitting the wall. The process is best illustrated on data from tokamak JET shown as a heatmap (figure 3.2) and separatrix lines before a thermal quench (figure 3.3).

Vertical Displacement Event (VDE) is a consequence of inherently unstable magnetic field for elongated plasma cross-sections. As a follow-up, large thermal loads and rise of halo currents are observed.

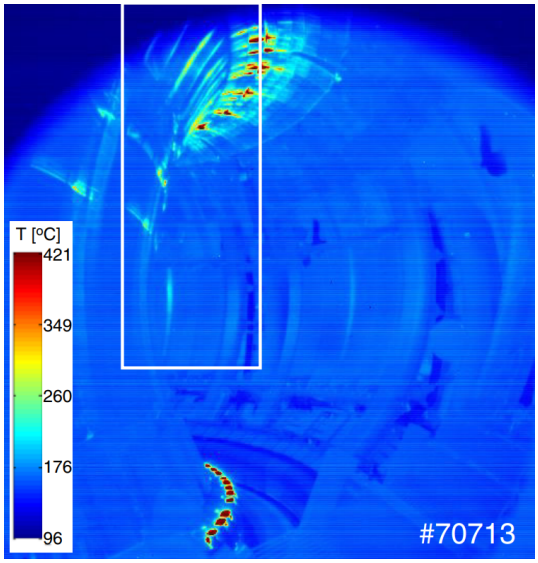

Figure 3.2: Heat map of plasma facing components for VDE at JET. Temperature increase is seen in the lower part (divertor) and the upper part of the chamber – caused by VDE. [9]

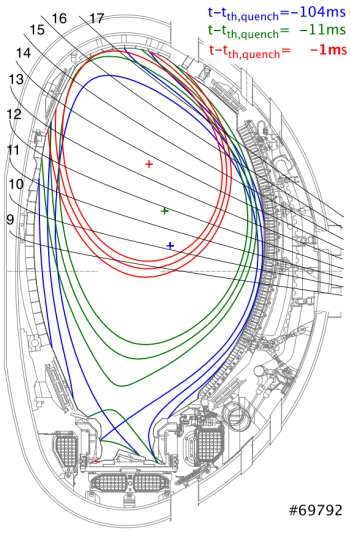

Figure 3.3: Reconstruction of magnetic equilibrium for VDE at different times before thermal quench. Data from tokamak JET. [9]

Halo current

It is a current which flows outside the confined plasma region in the scrape-off layer. The current in the layer can intercept a material surface, where taking the path of least resistance possibly causes intense heating and deformation of the material. [1]

Moreover, interaction of such magnetic field, caused by this current, and poloidal magnetic field results in a strong force acting on the whole vessel, possibly leading to the mechanical deformations.

3.1.1 Stabilization

VDE growth could be lowered using a conducting shell. This way the eddy currents are induced in the wall and poloidal flux is trapped between plasma and conducting wall. Magnetic tension caused this way compensates force causing the displacement. [10]

Another proven option of how to prevent such disruption is using system of active feedback. It monitors plasma movements in vertical direction and supplies current to the stabilization coils. By constantly receiving data, it adjusts magnetic forces thus keeping plasma vertically stabilized.

[1] `https://www.euro-fusion.org/glossary/halo-current/`, by EUROfusion, Halo current glossary entry.

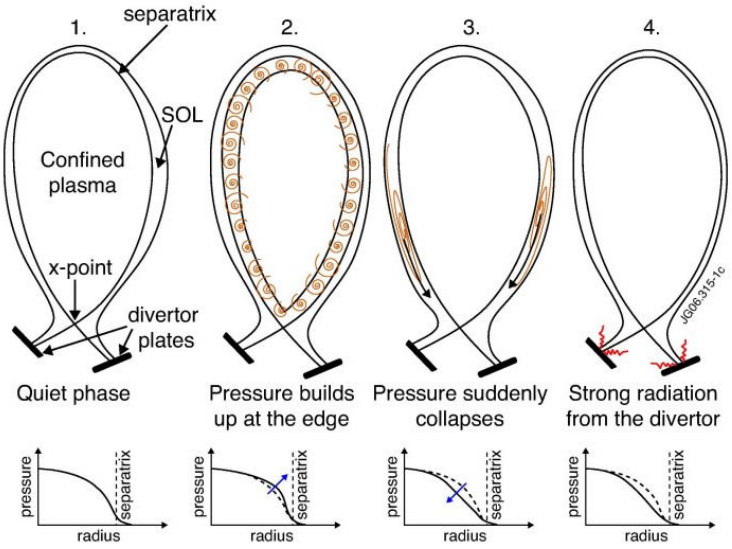

Figure 3.4: Time development of ELMs, illustrated on cross-section of plasma as well as radial pressure profile. [3]

3.2 Edge Localised Mode

Edge Localised Modes (ELMs) are common instability for H-mode operation. They cause drop of the pressure gradient, together with removing several percent of energy and particles stored in plasma. Their occurrence is both beneficial since they help stabilize pressure related disruptions, and inconvenient due to the possible damage of the divertor plates from large heat loads. [4]

The time development of ELMs is illustrated in figure 3.4, where upper plots show plasma escaping to the SOL and lower impact on radial pressure profile.

ELMs are categorized as 6 different types (I to V and Grassy), from which first three are the most common [4]:

- **Type I** have giant losses of energy via balooning modes, their frequency increased with heating power. However, this type is not important regarding confinement degradation.
- **Type II** require low T_{ped} and high p_{ped}, yielding good confinement and small energy loss.
- **Type III** occur at similar T_{ped} as type II, with relatively higher frequency. Disappear with increased heating and transit to type I.

[2] `https://www.euro-fusion.org/fusion/spot-on-jet-operations/maintaining-the-plasma/plasma-instabilities/`, by EUROfusion, Plasma instabilities - research for tomorrow's energy supply, spot on JET operations.

3.3 Disruptions

Disruptions are rapid losses of stability causing major breakdown of plasma and tension forces on surrounding structures. The instability is induced by fracture of magnetic surfaces, resulting in two processes:

- **Thermal quench**, loss of thermal energy, process lasting several ms at most,
- **Current quench**, slower loss of magnetic energy.

Not only could the above mentioned processes lead to damage of the tokamak components, they also provide suitable conditions for generation of RE.

3.4 Runaway Electrons

The generation of RE happens when the acceleration caused by the electric field is larger than the breaking by the opposing friction force. It can occur both in terrestrial, extraterrestrial or in artificial plasmas. An example of the process in nature is acceleration of electrons during flashes in thunderstorms. In tokamaks, RE generation can happen when the intensity of the electric field is increased, e.g. during the loss of plasma conductivity.

3.4.1 Derivation

The equation describing the process is derived from Fokker-Planck equation, stating the change of the momentum of electrons in one dimensional example as: [11]

$$\frac{\mathrm{d}}{\mathrm{d}t}\left(m_{\mathrm{e}0}v\right) = eE - C_e\psi(v/v_{\mathrm{te}}), \tag{3.1}$$

$$\psi(x) \equiv \frac{2}{\sqrt{\pi}x^2}\int_0^x \xi^2 e^{-\xi^2}\mathrm{d}\xi, \tag{3.2}$$

where $m_{\mathrm{e}0}$ is electron mass, v_{te} is thermal and v electron velocity, e elementary electric charge, E external electric field, C_e constant, $\psi(x)$ is Chandresekhar function.

The figure 3.5 shows dependency of a friction force on an electron velocity. It is a combination of collisional effects (Chandresekhar function) and radiative losses, compared to the accelerating electric force eE. When the friction force is greater than the electric force (up to v_{crit}), electrons are slowed. However, when the electron velocity reaches the critical value, they are accelerated to a pile-up zone (and not further due to the deceleration caused by radiative processes). This process is not fully described since collisional effects are calculated for non-relativistic electrons only.

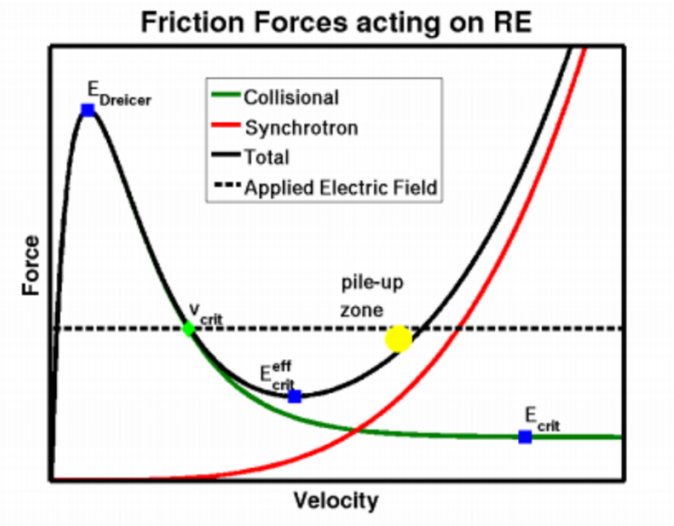

Figure 3.5: Friction force acting on electron depending on its velocity. Illustrated in arbitrary units according to the [12].

Moreover, the collisional force has its local maximum for small velocities in the form of Dreicer electric field E_{Dreicer} [11] :

$$E_{\mathrm{Dreicer}} = \frac{n_{\mathrm{e}} e^3}{4\pi\varepsilon_0{}^2 k_{\mathrm{B}} T_{\mathrm{e}}} \ln \Lambda. \tag{3.3}$$

If the intensity of electric field is larger than this value, RE are always generated.

3.4.2 Generation

Runaway electrons can be divided into two large groups according to their origin – primary (generated by applied electric field) and secondary (mostly generated by the interaction of primarily created RE and other thermal electrons). The processes can be explained in detail on a thermal Maxwellian distribution of electrons, plotted in velocity-space in figure 3.6.

3.4.3 Primary RE

- **Dreicer** The basic type of RE generation is acceleration of electrons by electric field, as discussed in section 3.4.1. Due to the diffusion processes in the velocity distribution (figure 3.6 top), initially slower electrons can reach the critical velocity and be severely accelerated.
- **Hot tail** When plasma is rapidly cooled by disruptions, velocity of the bulk of the electron is decreased. Since the cooling time of plasma is much shorter than the collisional time of the fastest electrons, they are not decelerated and remain in the hot tail. Moreover, as the temperature and conductivity decrease, intensity of an electric field is increased, which gives ideal conditions for RE generation.

3.4.4 Secondary RE

- **Avalanche** The already created RE can interact with thermal electrons present in plasma, transferring part of their energy, possibly large enough to get them into the runaway region.

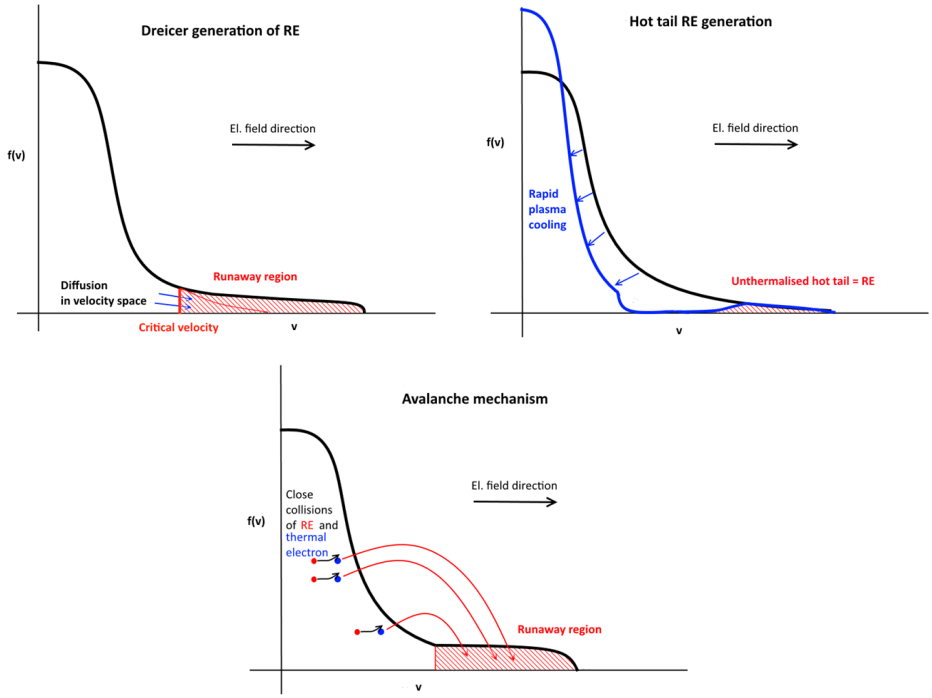

Figure 3.6: Images show velocity distribution of electrons according to different types of generation processes of RE [13]. Upper left figure is a classic Dreicer, upper right represents hot tail and lower avalanche mechanisms.

Chapter 4

Semiconductor Pixel Detectors

Silicon semiconductor detectors are widely used type of the solid-state detectors in HEP. Such detectors can have detection channels in strip (sensitive lines) or pixel (sensitive matrix) configurations. Their advantages relevant to the plasma experiments are fast readout, short dead time and radiation hardness.

The detection process in general requires ionizing radiation to produce electron-hole pairs in the sensor medium. Utilizing properties of semiconductors, electrons and holes drift to the opposite sides of the sensor, generating induced current.

Each of the detection elements (strips or pixels) is connected to an Application Specific Integrated Circuit (ASIC), in which a conversion from an analog current pulse to a digital signal is performed. Readout of the detector is ensured by a data acquisition system which provides communication to and from computer.

4.1 Interaction of Ionizing Radiation with Matter

Ionizing radiation is defined as radiation consisting of particles, X-rays, or gamma rays with sufficient energy to cause ionization in the medium through which it passes. It can be divided into two basic categories:

- **Direct ionization**, i.e. charged particles. The process of ionization happens directly via the Coulomb interaction.
- **Indirect ionization**, i.e. electromagnetic radiation and neutral hadrons such as neutrons. Secondary charged particles ionize the surrounding environment by a direct ionization.

Since detection of radiation relies on generation of a measurable electrical signal, particle detectors are primarily suited to detect directly ionizing radiation. Incident particles are slowed down via Coulomb interaction with electrons in the absorber material. According to the law of conservation of momentum, electrons in the absorber may receive enough energy to leave their ground state. This way, ionization of atoms of the semiconductor detector material occurs and electron-hole pairs are created.

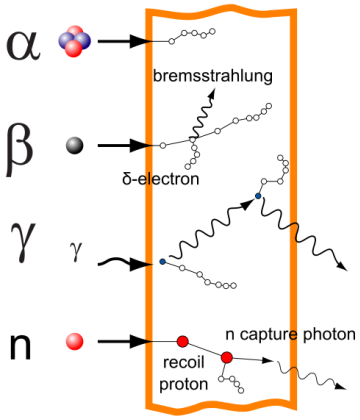

Figure 4.1: Illustration of interaction of ionizing radiation with matter.[1]

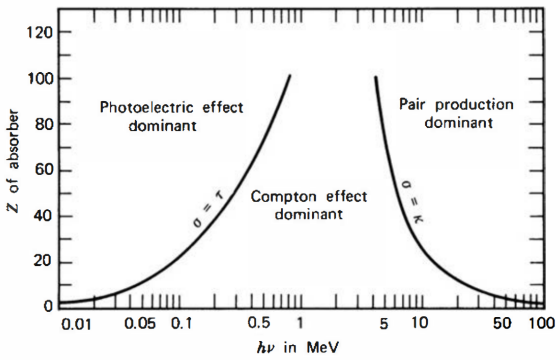

Figure 4.2: Dependence of photon-interaction processes on atomic number Z and photon energy $h\nu$. For silicon, photoelectric effect is dominant up to $\approx 70\,\mathrm{keV}$. [14]

Due to the differences in masses of incoming particles, interaction path for heavy charged particles and electrons differs. Since the transfer of energy is mostly focused towards the electrons in material, heavy charged particles ionize in a path without significant deviations. This is a straight consequence of momentum conservation. On the other hand, for the incident electrons having the same mass as absorber electrons, their path may considerably deviate.

It is possible to detect even indirect radiation, though it must generally undergo catastrophic interaction – radically altering its properties. [14] That means creation of secondary particles such as electrons for X– or gamma rays or heavy charged particles for neutrons. Products of these processes then interact via direct ionization mentioned above. For these purposes, semiconductor detectors are either equipped with either thicker silicon, cadmium telluride or galium arsenide sensor (detection of X– rays) or conversion layer with low atomic number (neutron detection).

Simplified diagram of different interactions is in figure 4.1, illustrating all of the above mentioned ionizing processes.

4.2 Interaction of fast electrons

As the main topic of this work is directed towards RE diagnostics, interactions of electrons with material are discussed more thoroughly.

Fast electrons lose their energy via two main processes [14]:

- **Radiative**, in which electrons lose energy in form of electromagnetic

[1] `https://commons.wikimedia.org/wiki/File:Strahlenarten_en.svg` by Napy1kenobi, CC BY-SA 3.0

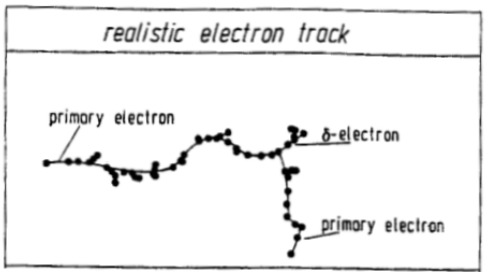

Figure 4.3: Schematic view of realistic electron track (lower figure). [16].

radiation. The specific energy loss is described as

$$-\left(\frac{\mathrm{d}E}{\mathrm{d}x}\right)_r = \frac{NEZ(Z+1)e^4}{137{m_{\mathrm{e}0}}^2c^4}\left(4\ln\frac{2E}{m_{\mathrm{e}0}c^2}-\frac{4}{3}\right). \tag{4.1}$$

- **Collisional**, due to ionization and excitation, derived by Bethe as

$$-\left(\frac{\mathrm{d}E}{\mathrm{d}x}\right)_c = \frac{2\pi e^4 NZ}{m_{\mathrm{e}0}v^2}\left(\ln\frac{m_{\mathrm{e}0}v^2E}{2I^2(1-\beta^2)} - (\ln 2)\left(2\sqrt{1-\beta^2}-1+\beta^2\right)\right.$$
$$\left.+(1-\beta^2)+\frac{1}{8}\left(1-\sqrt{1-\beta^2}\right)^2\right). \tag{4.2}$$

In these equations, N and Z are number density and atomic number of absorber, I is the effective ionization potential, e and $m_{\mathrm{e}0}$ are electron charge and mass, and β ratio of speed of the particle v to the speed of light c. They both describe stopping power S $(\equiv -\,\mathrm{d}E/\,\mathrm{d}x)$, defining how much energy does incident particle lose when passing through absorber medium.

Resulting stopping power for electrons is defined as a sum of (4.1) and (4.2)

$$\frac{\mathrm{d}E}{\mathrm{d}x} = \left(\frac{\mathrm{d}E}{\mathrm{d}x}\right)_r + \left(\frac{\mathrm{d}E}{\mathrm{d}x}\right)_c, \tag{4.3}$$

with their ratio being approximately $S_{\mathrm{r}}/S_{\mathrm{c}} \simeq EZ/700$, where E is in MeV. [14]

For electron energies in the order of MeV, the radiative processes represent only a small fraction, being more dominant for absorbers with high atomic number.

4.2.1 Absorption

Great part of the electron interactions is causing only minor energy losses and small deviations, sporadically ejecting δ-electrons accompanied by larger scattering angle and energy loss. [15] The illustration of the realistic track of energetic electron in material is in figure 4.3

This causes the electrons to rapidly change direction in the medium even for a thin absorber, best approximated by definition of absorption coefficient μ_a as

$$\frac{J}{J_0} = e^{-\mu_a h}, \tag{4.4}$$

where J_0, J is counting rate without and with absorber, respectively, and h is absorber thickness in units $g\,cm^{-2}$. [14]

4.2.2 Backscattering

For smaller energies and larger atomic number of absorber, a backscattering can occur accompanied by minimal deposition of energy and scattering angle larger than 90°.

4.3 Interaction of gamma rays

The measurements in this work were focused on the detection of secondary photons, therefore the processes of their interaction (Compton scattering, photoelectric absorption and electron-positron pair creation) are described in more detail. The figure 4.2 shows which processes are dominant in dependence on atomic number Z of an absorber and different photon energies $h\nu$.

4.3.1 Photoelectric absorption

As clearly seen in the figure 4.2, this process occurs for low energy photons. Their energy is absorbed in one of the electrons in the inner shell of the atom. If it is larger than the binding energy E_{be} of absorber electron, the electron is ejected with kinetic energy E_e

$$E_e = h\nu - E_{be}, \tag{4.5}$$

where h is Planck constant and ν frequency of photon. After undergoing this process, the liberated electron may interact with other electrons in the sensor material, generating signal for the detector.

Moreover, the ionization creates a vacancy in the inner shell of the atom, which is filled with electron from one of the higher shells. This is accompanied by releasing the energy difference either in the form of characteristic radiation or Auger electrons. [14]

Absorption edges

Since the energy of incoming photons must exceed the electron binding energy, an increase of cross section for the interaction is observed at such point. Moreover, as the electron binding energies are different for each of the electron shells (innermost one being K-shell), each material has multiple absorption edges.

The illustration of K-edges for silicon is in figure 4.5.

Characteristic radiation

As this radiation occurs when electron from higher shell transients to a lower shell, different energy is released for each element of the periodic table. This process is governed by principles stated by quantum mechanics, thus transitions may occur from different degenerate levels to a lower state, producing characteristic radiation.

Notation of the atomic spectral lines is similar to the nomenclature of the absorption edges, with an addition of different transitions (greek letters comparing shell levels and numbers stating degeneration level) – visualized in figure 4.6.

4.3.2 Compton scattering

Instead of being fully absorbed, the incoming photon is deflected on either free electron or one in an outer shell of the absorbing material. This results in the creation of a recoil electron and photon at scattering angle θ, due to the conservation of energy and momentum. The energy of the scattered photon is calculated as

$$h\nu' = \frac{h\nu}{1 + \frac{h\nu}{m_{e0}c^2}\left(1 - \cos(\theta)\right)}, \tag{4.6}$$

where h is Planck constant, ν is initial and ν' final frequency of the photon, $E_{e0} = m_{e0}c^2$ is a rest-mass energy of electron.

Differential cross-section of photon scattering is given by Klein-Nishina formula. For low frequencies, Thomson scattering is given, for higher ones, Compton scattering. Figure 4.4 gives distribution of scattering angles for different energies.

4.3.3 Electron–positron pair creation

For higher photon energies, cross sections of both photo-effect and scattering become low. However, if the energy exceeds twice the rest-mass of electron ($2E_{e0} = 1022\,\mathrm{keV}$), the photon can be converted into an electron-positron pair. The excessive energy is distributed in a form of kinetic energy of created electron and positron. Shortly after creation, the positron undergoes annihilation, releasing gamma radiation.

4.3.4 Photoneutrons

If the energy of the photon exceeds the value of neutron binding energy in the atomic core, a neutron expulsion may occur. The necessary photon energies are in the order of MeV, table of cross-sections for different elements can be found in [18].

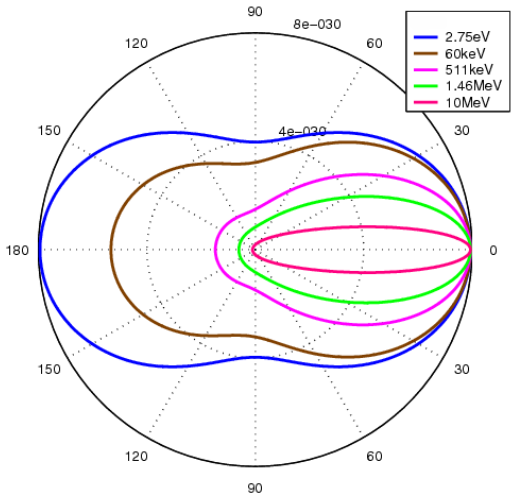

Figure 4.4: Compton effect distribution of different scattering angles for different impact photon energies. Illustrated according to [17].

4.3.5 Mass Attenuation coefficient

All above mentioned processes contribute to the probability of a photon interacting within absorber medium. It is best described by mass attenuation coefficient μ_m, comparable to the cross section of absorption, though defined per unit mass, not per particle. The value is defined as

$$\mu = -\frac{1}{J}\frac{\mathrm{d}J}{\mathrm{d}x}, \qquad \mu_\mathrm{m} = \frac{\mu}{\varrho_\mathrm{m}}, \tag{4.7}$$

where μ is linear attenuation coefficient defined as decrease of rate J per length and ϱ_m is mass density. For the larger values of the coefficient μ_m, photons are more easily stopped by the material.

Example of the dependency of this coefficient on the photon energy is shown in figure 4.5. Different processes and their contribution are also visualized.

4.4 Physics of semiconductors

In principle, semiconductors can be used as intrinsic – made of pure element in a crystalline lattice, usually from IV.A group in periodic table (silicon, germanium or diamond).

They are used as detectors due to their characteristic energy bands. For low temperature, all of the valence electrons are bound in the lattice, however, when the temperature rises (or after passage of an ionizing radiation), the covalent bond may break. This creates a free electron and a hole available for conduction.

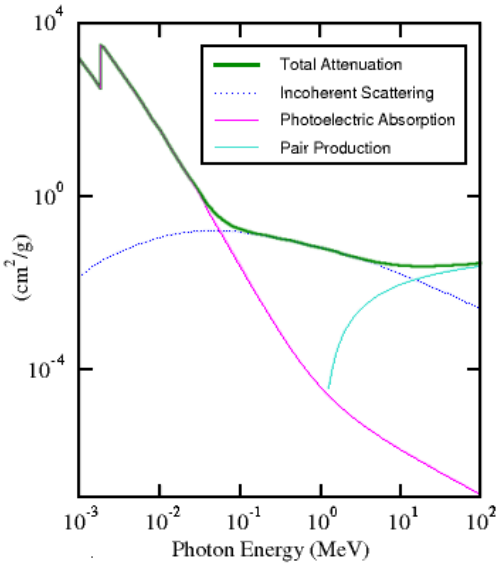

Figure 4.5: Dependence of silicon mass attenuation coefficient μ_m on photon energy. Regions with dominance of different effects are visible (photoeffect for $E < 100\,\mathrm{keV}$, Compton effect for E from $0.1\,\mathrm{MeV}$ to $10\,\mathrm{MeV}$ and pair creation for $E > 10\,\mathrm{MeV}$). K-edge of silicon is seen as a steep attenuation increase at $E = 1.84\,\mathrm{keV}$. [19]

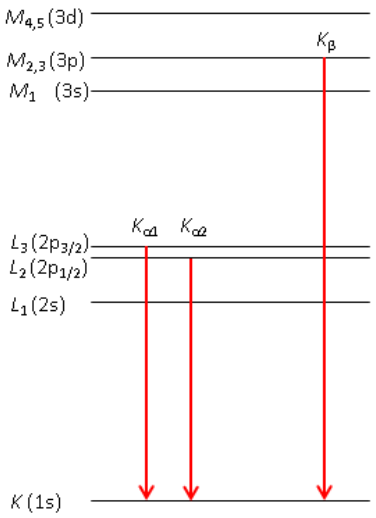

Figure 4.6: Different types of characteristic radiation. Red arrow represents filling of electron vacancy in the inner K shell from upper shells. It is accompanied by releasing the energy difference, by a photon with defined frequency ν.

Occupation probability of state $F(E)$ is defined by Fermi-Dirac distribution

$$F(E) = \frac{1}{1 + \exp\left(\frac{E - E_\mathrm{F}}{k_\mathrm{B} T}\right)}, \tag{4.8}$$

where k_B is Boltzmann constant, T absolute temperature and E_F Fermi level – energy at which the occupation probability of state is half. [20] For intrinsic semiconductor, E_F is close to the middle of the band gap.

Difference between insulators, semiconductors and conductors is in figure 4.7, shown as an energy structure for valence and conduction bands. For silicon, the band gap voltage is $E_\mathrm{gap} = 1.12\,\mathrm{eV}$, however, due to electron momentum in bands a mean energy of $E = 3.6\,\mathrm{eV}$ is needed per electron-hole pair creation.

A thermally or radiatively created pair recombines shortly after and would not be detected at all. As a countermeasure, elements with higher (donors, n-type) or lower (acceptors, p-type) number of valence electrons are doped into the substrate. The acceptors are usually from III.A group (boron, aluminium) and donors from V.A group (arsenic, phosporus).

Implanting shifts levels of both valence and conduction bands in respect to the Fermi energy. For donors, conduction band is closer and vice-versa for acceptors. Moreover, usage of both types creates a p-n junction at their interface.

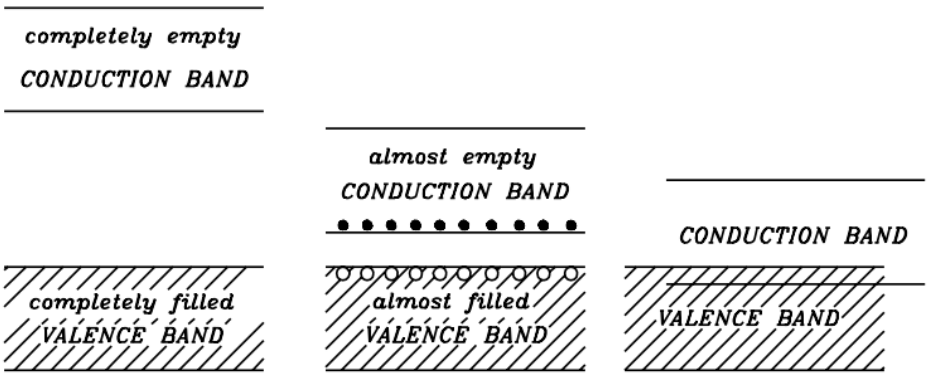

(a) : Insulator.

(b) : Intrinsic semiconductor.

(c) : Conductor.

Figure 4.7: Comparison of insulator, semiconductor and conductor as energy structure of valence and conduction bands. Black and white circles represent electrons and holes, respectively. [20].

4.4.1 P-N junction

Creation of a junction is illustrated in figure 4.8a. Due to different electric charges, a drift of charge carriers occurs resulting in recombination. This process lasts until diffusion current exactly cancels the drift, resulting in built-in voltage V_{bi} defined as difference between acceptor $E_{\mathrm{i^p}}$ and donor $E_{\mathrm{i^n}}$ energy levels

$$V_{\mathrm{bi}} = \frac{1}{e}\left(E_{\mathrm{i^p}} - E_{\mathrm{i^n}}\right) = \frac{k_{\mathrm{B}}T}{e} \ln \frac{N_{\mathrm{A}} N_{\mathrm{D}}}{{n_{\mathrm{i}}}^2}, \tag{4.9}$$

where N_{A}, N_{D} are doping concentrations of acceptors and donors, n_{i} intrinsic concentration and elementary charge e. [20]

This region without any free charge carriers is called depletion or space charge region and can be further expanded to increase active volume of the detector.

Depletion region

The depletion region not only counteracts the diffusion of electrons and holes moreover any new charge carrier pairs that are created within the region drift in the direction of gradient of the electric potential. This generates a signal that can be measured using appropriate electronic instrumentation. Since electron-hole pairs are also created thermally, detectors always measure some noise, represented by a dark current.

Bias voltage

Since the natural depletion region is small (order of µm) in comparison to the whole sensor volume (hundreds of µm), in order to expand it a reverse voltage is usually applied to the pn junction. The resulting thickness d of

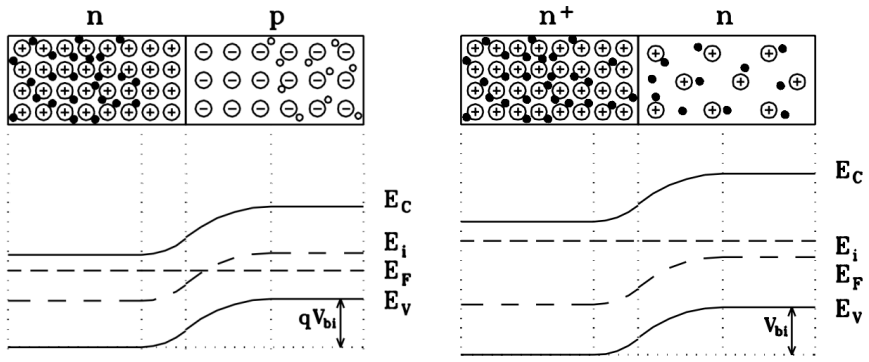

(a) : p-n junction **(b) :** n-n+ junction

Figure 4.8: Schematic of substrate junctions in thermal equilibrium. Electrons and holes are black, respectively white circles. Profiles of conduction E_C and valence E_V bands, together with Fermi E_F and built-in E_i level (causing lining-up of Fermi levels in thermal equilibirum).[20]

depletion region can be calculated as a function of reverse bias voltage V_b

$$d \cong \left(\frac{2\varepsilon V_b}{eN_{im}} \right)^{1/2}, \tag{4.10}$$

where ε is absolute permitivity and N_{im} lower dopant concentration at the junction. [14]

Applying higher voltage enhances speed of propagation of charge carriers, however, the value cannot be increased infinitely as a breakdown may and will occur.

Capacitance

Due to different electric potentials around the junction, a junction capacitance can be measured

$$C \doteq \varepsilon \frac{A}{d} \cong A \left(\frac{q\varepsilon N_{im}}{2V_b} \right)^{1/2}, \tag{4.11}$$

where A is area of depletion region.

Ideally, the capacitance should be as low as possible, which correlates with thicker depletion region thus more sensitive volume. It also helps with distinguishing signal from noise.

By measuring capacitance-voltage characteristics, a value of bias voltage can be obtained at which the sensor is fully depleted. For small values of reverse voltage, capacitance is decreasing as the depletion thickness d is increased according to (4.10). When the value of capacitance saturates, sensor is fully depleted.

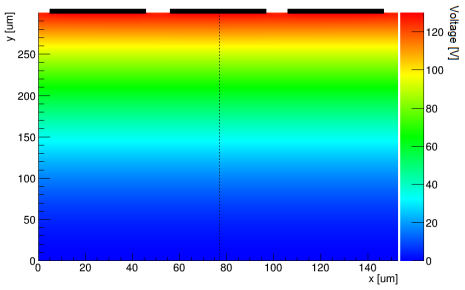

(a) : Linear electric field for three strips. Bias voltage $V_b = 150\,V$, depletion voltage $V_{dep} = 100\,V$.

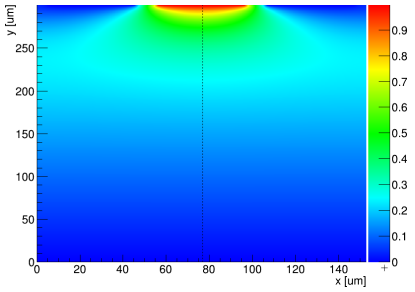

(b) : Weighting potential calculated for specified configuration.

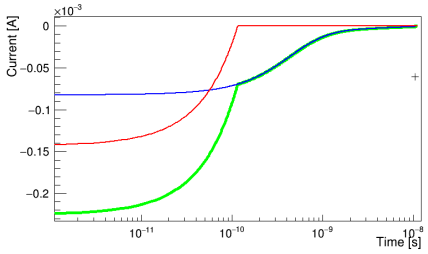

(c) : Signal of front-illuminated sensor with 5 MeV alpha particles.

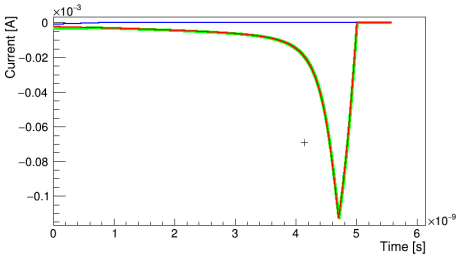

(d) : Signal of back-illuminated sensor with 5 MeV alpha particles.

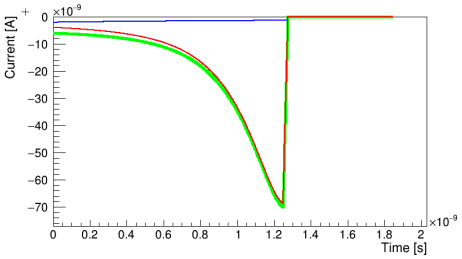

(e) : Signal of front-illuminated sensor with 100 keV X-ray. Photon interacted 100 µm in the sensor.

Figure 4.9: Simulation of signal formation in silicon detector using Wakefield2 [21]. Thickness of sensor is 300 µm. Green line represents total signal, contribution from electrons and holes red, respectively blue.

Typical configuration

Even though the ideal substrate would be intrinsic with high resistance, a p- or n- type substrates are typically used. This is mostly caused by high price and difficulties in factory processing of pure silicon ingots.

For n-type substrate, a p^+ implant is used to create junction. Higher concentration (thus the plus sign) has to be doped in order to counteract the n-type impurities.

On the opposite side an implant of n^+ is used so as to connect the sensor to conductor and ensure desired configuration of electric fields. The junction between n^+ implant and n-type substrate is visualized in figure 4.8b and is similar for p^+ in p-type substrate.

4.4.2 Signal measurement

The formation of signal is determined by the movement of charge carriers in substrate towards the implants. The resulting signal then needs to be captured and processed by the electronic ASICs.

Shockley-Ramo theorem

As was proven by [22] and [23], the induced current i from moving charges between electrodes is calculated as

$$i = qvE_{\mathrm{v}}, \tag{4.12}$$

where E_{v} is component of electric field in the direction of velocity v of charge.

Since segmented detectors have more than one collector electrode, the signal heavily depends on the position of moving charges. Shockley-Ramo theorem is applied to set a unity potential to the selected electrode and zero to others. This yields weighting potential $\mathbf{E}_{\mathrm{w}}$, thus the induced current i at the electrode is

$$i = q\mathbf{E}_{\mathrm{w}} \left(\sum_j \mathbf{v}_{j,\mathrm{e}} + \sum_j \mathbf{v}_{j,\mathrm{h}} \right), \tag{4.13}$$

where indices e and h denote electrons and holes, respectively, and j is summing index over all created pairs. [23] Simulation of applied electric field and resulting weighting potential is shown in figures 4.9a and 4.9b.

Time development of the induced current i for different signals is visualized in figures 4.9c, 4.9d and 4.9e. It is clearly visible that the response of detector heavily depends on geometry and dominant charge carrier type.

Electronics

The whole process of capturing generated signal can be very complex due to the typical signal amplitude being in the order of fC, however, some general components are very similar in all devices.

As a first step, a charge-sensitive amplifier is used, producing voltage output proportional to the input current. This value is then processed in a desired way (e.g. measuring height of the signal, time of arrival, ...) and converted to a digital value using Analog-Digital Converter (ADC).

One of the most commonly used global parameters which control overall detector response is discriminator level – THreshold Low (THL). Signals above THL are considered to be above instrumental noise. The desired value is set in the computer and converted using Digital-Analog Converter (DAC), resulting voltage is supplied to the comparator – electronic part that compares input and reference signals.

The electronic design has to consider different effects caused by the factory processing, therefore number of variable parameters are usually included in the hardware design. This ensures an uniform response of the detector, e.g. trimming the setting of comparator in each pixel.

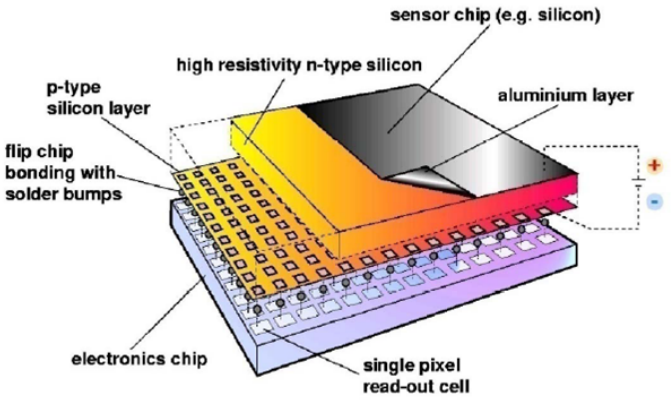

Figure 4.10: Cross-section of a hybrid pixel detector [24]. The figure illustrates silicon senor covered with alumium layer (due to biasing), connected to the Medipix2 ASIC via bump-bonds.

4.5 Medipix2

Medipix2 is a hybrid pixel detector primarily designed for photon-counting X-ray imaging. It was developed by the Medipix2 collaboration at CERN. The single chip has 256×256 pixels with pitch $55 \times 55\mu m^2$, larger coverage area can be achieved by a combination of 4 chips as is shown in the figure 4.11a, this configuration is called "quad". [24]

4.5.1 Readout

Because of the need for a new and flexible interface, a CoaXPress readout has been developed at FNSPE CTU. [25] It serves as an interface between the detector and a computer, ensuring proper operation and data streaming. The Medipix2 quad detector is mounted on a Printed Circuit Board (PCB) with large heat-sink, connected with motherboard via 4 flat cables (each of them can be up to 1 m long).

The main advantage of this readout is usage of a coaxial cable between setup and computer, which provides around 100 Hz operation - maximum for the Medipix2 chip. The dead time needed for the chip to process the signal and transfer data is $100\,\mathrm{MHz}/(256 \times 256 \times 14)$, 14 representing number of bits in each of the pixels. Framerate therefore depends on the width of the acquisition window.

4.5.2 Software

As a mean of controlling the setup from computer, Adapted Software for PIxel REadout (ASPIRE) has been developed by the author of this work [26], based on the work of [27].

The software is a complex work using Qt libraries [2], providing number of interfaces used for detector operation. It gives options of data taking with

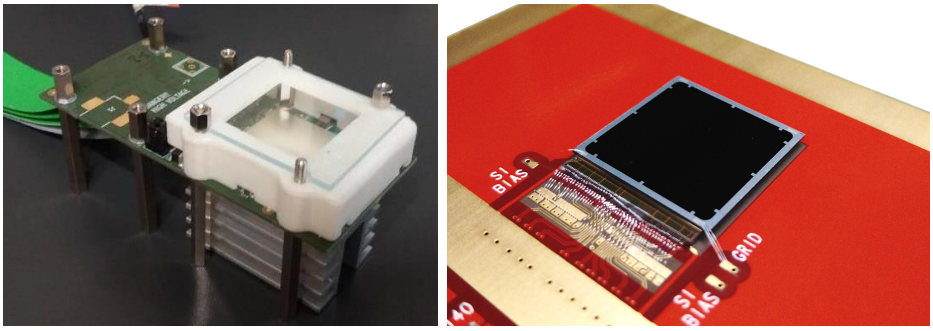

(a) : Medipix2 quad detector. **(b) :** Timepix3 detector.

Figure 4.11: Used semiconductor pixel detectors.

specified acquisition window, visualization of data frames and management. Moreover, it enables user to calibrate pixel response and set different DAC values, the most important being THL.

4.5.3 Equalization

One of the important functions of the software is equalizing pixel response. As mentioned in chapter 4.4.2 each pixel may respond differently to the same signal. Therefore 3 trim bits in each pixel comparator exist, enabling fine tuning of the response.

ASPIRE solves this inequality during a procedure in which all the pixels are monitored according to the different threshold setting. After starting the procedure, a specified range of the detector THL is scanned for two different values of local trim bits - all set as zeros and ones. By doing so, the response to the noise edge of each individual pixel is gained at different THL value, which is stored.

Since some pixels may be completly damaged and therefore being noisy (always producing signal) or dead (never producing signal), the equalization procedure may mask them by setting different mask bit value.

The algorithm then calculates the best possible combination for trim values using the equations

$$\overline{adj_{i,j}} = 7 - \left\lceil \frac{THL_{i,j} - \mu_{\min}}{\mu_{\max} - \mu_{\min}} \right\rceil, \quad \overline{\overline{adj_{i,j}}} = \left\lceil \frac{\mu_{\max} - THL_{i,j}}{\mu_{\max} - \mu_{\min}} \right\rceil \tag{4.14}$$

$$adj_{i,j} = \left| \frac{\overline{adj_{i,j}} + \overline{\overline{adj_{i,j}}}}{2} \right| \tag{4.15}$$

where $\mu_{\max}$, $\mu_{\min}$ are means of the low and max distributions and is THL_{ij} is THL value at which the pixel reached the noise level. The result is then averaged. The result is a 3 bit *adj* individual value, set for each pixel. The result of a successful equalization for Medipix2 quad is shown in the figure

[2] `http://doc.qt.io/qt-5/reference-overview.html` by Qt Company Ltd., GNU Free Documentation License version 1.3

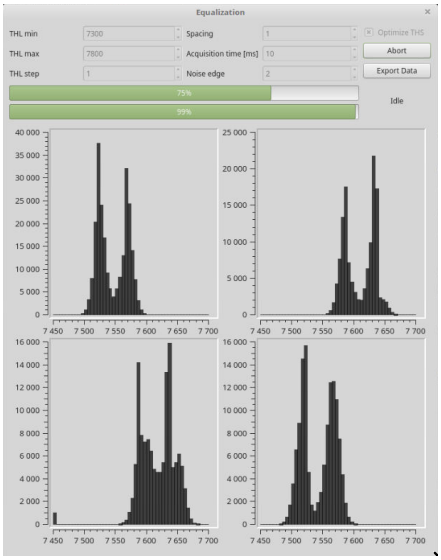

Figure 4.12: Finished equalization of Medipix2 Quad detector. Each of the subfigures represents number of pixels that reached noise edge depending on THL, for each chip. The two distributions are for different settings of $adj = 0$ (left) and $adj = 7$ (right). The resulting configuration is obtained by setting each pixel response according to the 4.15. [26]

4.12, its effect visualized on an X-ray image of Dual In-line Memory Module (DIMM) in figure 4.13.

4.6 Timepix3

Similarly to Medipix2, Timepix3 is an ASIC developed by Medipix3 collaboration at CERN in 130 nm technology, it has 256×256 pixels with pitch 55×55 µm^2. It is a newer version, with a more functionality, mostly focused for acquiring timing information – Time of Arrival (ToA) and Time over Threshold (ToT), with the latter providing energy deposition information. [28]

The main difference of generation 3 is simultaneous recording of ToT and ToA, in addition to a so-called data driven mode – pixels send the signal only when detected. This enables the detector to stay sensitive most of the time, limited by read-out bandwidth.

4.6.1 Readout

Nikhef laboratory developed a general purpose readout system called SPIDR, which can also accept and time stamp an external trigger pulse. Packets of information are sent via ethernet cable in 64 bit bunches. Maximal transfer rate is 80 MPix/s. [29]

The data is transferred in a raw format, without being ToA sorted. The author of this work developed a data-processing software which combines input

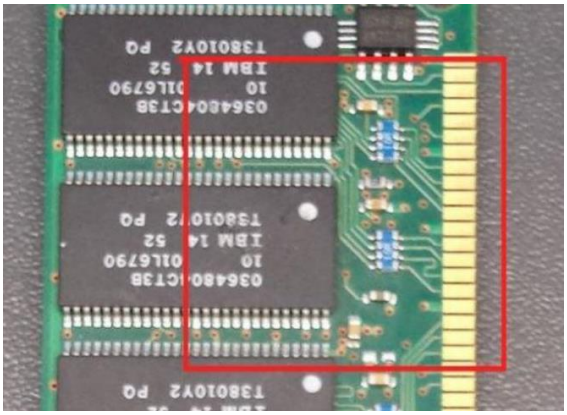

(a) : Image of DIMM.

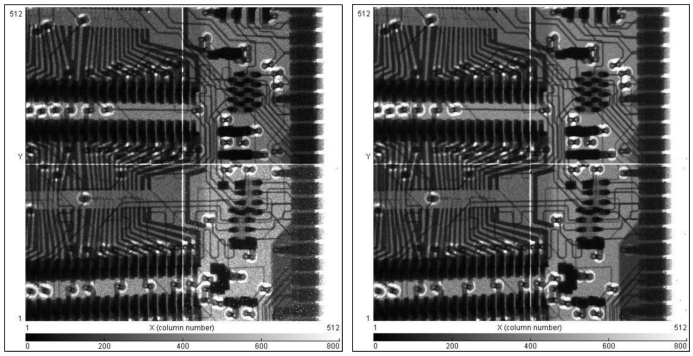

(b) : Without equalization. **(c) :** With equalization.

Figure 4.13: Equalization effect on usage of Medipix2 quad detector. Image of DIMM with and without equalization. Noise is distinctly larger in the figure without equalization, this can be seen the most easily in the lower right chip of both quad sensors.

files, sorts the inputs according to the ToA, locates clusters and generates Comma-Separated Value (csv) file for further analysis.

4.6.2 Time-walk calibration

The calibration of the device was done by the author of this work on Velocity Map Imaging (VMI) experiment, published as [30]. A laser interacts with molecule which breaks to ions and electrons, which are then accelerated towards the phosphorus screen and are converted to light. That signal is recorded by Timepix3Cam [3] and saved for data processing.

In Timepix detectors, the shape of the signal corresponds to charging of a capacitor which is then slowly discharged using constant current. This results in a fixed falling edge, regardless of the maximal voltage, however, the rising edge is a bit steeper for higher voltage. Due to this fact a time-walk effect occurs best described in figure 4.14. As the rise time is similar for all energies,

[3] device with lenses, Timepix3 chip and sensor which interacts with visible light `https://www.tpxcam.org/`, Svihra

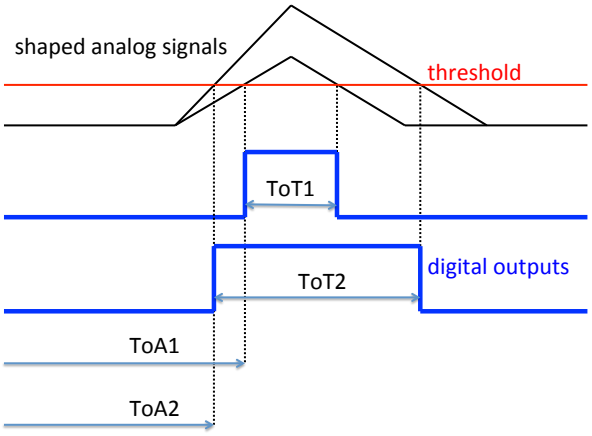

Figure 4.14: Signals have similar rise time, therefore larger ones cross THL earlier, resulting in earlier ToA. [30]

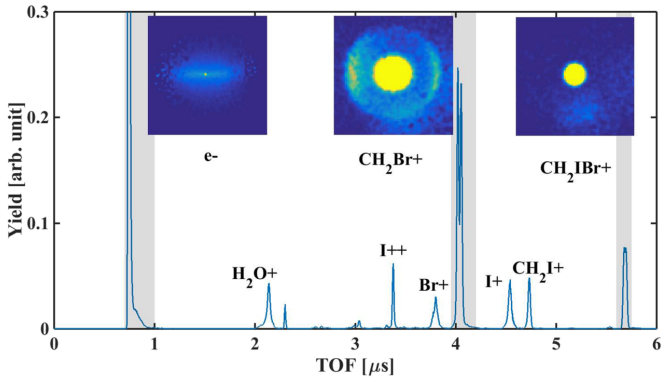

Figure 4.15: Ion Time of Flight (ToF) spectrum from VMI experiment with spatial information of particle information. [30]

the interactions that occured at the same time are registered with different ToA. Difference in the ToT then enables correction of such effects.

The calibration was therefore made using correlation of ToF ($ToF = ToA - triggerTime$) and ToT, together with centroiding, as interaction of light from both electrons and ions creates clusters in the sensor. The raw ToF data are visualized in figure 4.15, showing both spatial and temporal information from the detector. Comparison of the applied corrections is shown in figure 4.16 on the electron (e-) and double ion peak (CH_2Br+) as ToT vs ToF dependency.

The resulting improvement is in the figure 4.17, the sigma of gaussian fit for the double ion peak improved by almost a quarter. It also shows that the data quality may be greatly improved using taken data.

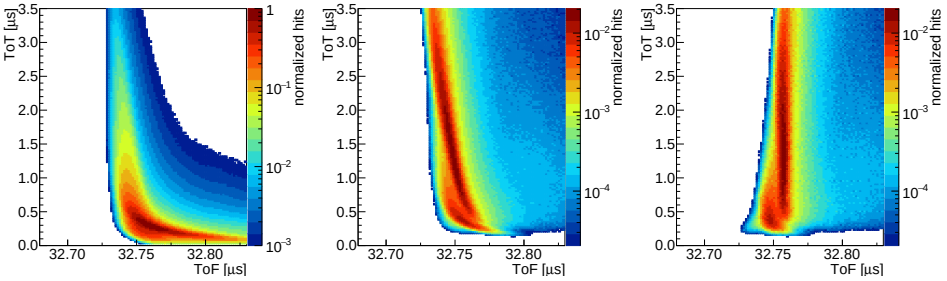

(a) : Electrons in raw data.

(b) : Electrons after centroiding.

(c) : Electrons after centroiding and ToT correction.

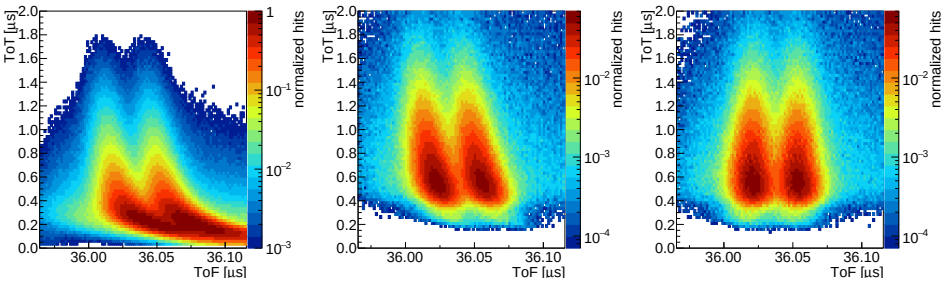

(d) : Ions in raw data.

(e) : Ions after centroiding.

(f) : Ions after centroiding and ToT correction.

Figure 4.16: ToT and ToF correlation for electrons and ions before and after centroiding and ToT correction. [30] It is visible that the calibration method improved the detector precision for ToF.

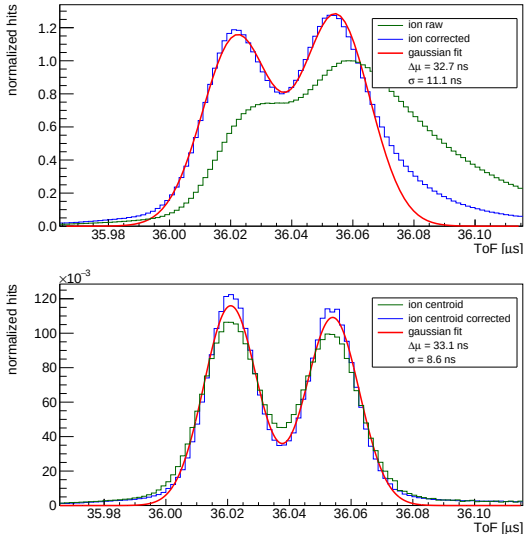

Figure 4.17: Plots illustrates ToF ion data taken at the VMI experiment. Upper plot shows effect of ToT calibration on time resolution of raw data, further improved by centroiding in the lower plot. [30] The sigma for the combined gaussian fit of double peak improved from 11.1 ns to 8.6 ns for ToT corrected and corrected and centroided data, respectively.

Chapter 5

Simulations of ionizing radiation interaction

Numerical simulations in general are a useful tool to model any process that cannot be solved analytically or would be too time consuming to do so. Currently, almost every field of study needs a testing on their hypotheses before constructing an experiment or to compare data to complex models.

In physics, simulations are commonly used to predict and help interpret results or model different types of physics experiments according to the current knowledge. Such simulations are mostly based on Monte Carlo method – mathematical approach using sequence of random numbers to solve a problem. For the reliability of the methods, a clear comparison between them and either analytic solutions or experimental data has to be observed. This is shown as a basic diagram representing relations of experiment, theory and simulation, see 5.1.

5.1 Monte Carlo simulations of ionizing radiation interaction

Monte Carlo methods rely on generating random numbers which are compared to user defined processes, usually interpreted as calculation of an integral or a cross-sections. For this purpose a large number of generations has to occur, slowly converging towards the result.

In principle, it is not the best possible solution to a number of problems as for small complexities an analytic solution could be more suitable. However, in simulations of transport of particles, Monte Carlo becomes more advantageous as the usage of different shapes and materials makes deterministic or analytical approach practically impossible. This is illustrated in figure 5.2.

The transportation processes are generally simulated with variable stepping length (dependent on particle type and absorber material), calculating probability of interaction in each of them. The resulting process yields energy deposition, particle tracks and even catastrophic interactions such as secondary particles or radioactive decay with all possible by-products.

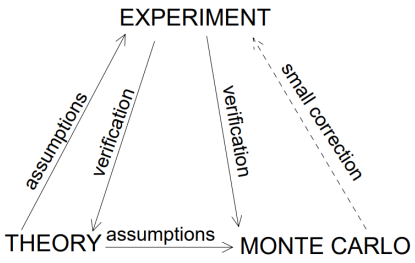

Figure 5.1: Relations of experiment, theory and Monte Carlo simulations. [31]

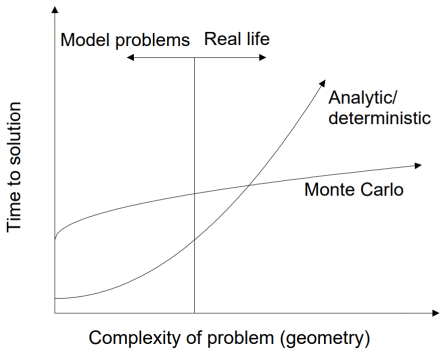

Figure 5.2: Time comparison of Monte Carlo and analytic approach to simulate particle transport in material. [31]

5.1.1 Toolkits

Due to the complexity of required simulations, a number of collaboration-developed toolkits already exist and are available. The advantage of their usage does not lie only in the ease of approach, much more in the accuracy of resulting models as they are comparable to data from many different experiments.

Some of the most known and widely used general toolkits include:

- **MCNP** Monte Carlo N-Particle, models particle transport and material activation, [32]
- **FLUKA** FLUktuierende KAskade, development of HEP detectors, [33], [34]
- **Geant4** GEometry ANd Tracking, used for particle tracking. [35]

GEANT4 toolkit was used for the purposes of simulating tokamak COMPASS, therefore its more detailed description follows.

5.2 Geant4 [35]

GEANT4 is a set of C++ libraries, specifically developed for simulations of interaction of ionizing radiation with matter. In comparison to the other tools for such purpose, GEANT4 has to be locally compiled in order to use its features.

This tool was used for simulating all of the CERN large experiments (ATLAS, ALICE, LHCb, CMS) and even number of space telescopes, modules and space stations, as well as space dosimetry. Furthermore, GEANT4 is being applied to model low energy experiments in nuclear medicine.

5.2.1 Description

In order to devise a simulation model, code has to implement:

- **physics list** defining interactions of interest,
- **detector construction** describing whole physical region together with the sensitive parts intended to analyze data,
- **run action** setting the particle types, energies and distributions.

Afterwards, the user can use either graphical/console interface to manually generate particles or predefined macros to automatize the process. The usage of macros enables running the code only once, reducing one of the most CPU intensive process - generating models and materials.

5.2.2 Physics list

Geant4 contains description of most of the known physical processes, ranging from low energy photon interaction up to the energies of quark-gluon plasma and proton-proton collisions.

At the beginning of the simulation, user has to choose which of these interactions are desired in his model, in general, the physics list could be constructed containing all possible types of interactions in any range of energies. Such simulation would take significant amount of time, therefore a reasonable choice of the processes has to be made.

The implementation can be done as an adaptation of virtual functions, where the user needs to specify each type of particle and interaction that are in the model. However, for easier interaction, number of reference lists have been deployed, some of them are

QGS Quark gluon string model, $E > 20\,\mathrm{GeV}$,

FTF Fritiof Model, $E > 10\,\mathrm{GeV}$,

BIC Binary Cascade Model, $E < 10\,\mathrm{GeV}$,

BERT Bertini Cascade Model, $E < 10\,\mathrm{GeV}$,

HP High Precision Neutron Model, $E < 20\,\mathrm{MeV}$,

These physics lists are primarily useful in HEP, for a more specific ones such as low energy electromagnetic radiation, Low Background Experiments (**LBE**) or Livermore physics models (**EMLivermore**) are implemented. All known physical processes are part of the above mentioned models, including the ones described in the previous chapter.

To reach desired simulation resolution, different lists can be combined in an user defined class UserPhysicsList. For the purpose of this work a standard **BERT** physics list containing electromagnetic processes has been utilized.

Another important parameter that impacts the resolution of the simulation is a production cut for interactions. In principle, Geant4 can simulate

propagation of all secondary, tertiary,... particles, though resulting in longer simulation time. By setting a cut, secondary particles are generated only above the cut-off energy defined using either energy or distance that the particle needs to be able to travel. The value set as a distance is automatically converted to different material-specific energies.

5.2.3 Detector Construction

Definition of 3D objects, forms and their materials is either manually implemented or imported from Geometry Description Markup Language (GDML).

Construction has to include world volume, which initiates maximal region and its background material. All other models are contained within the world volume and cannot overlap with each other. The overlaps would cause problems as the tracking of the particles happens in discrete steps, moreover the model would not be able to choose the correct object material.

All other models present in the simulation are then defined in three steps – solid, logical and physical, with any type of material.

materials

A set of already defined materials can be used, containing commonly used ones.

Since applications could be very specific regarding construction of either detectors, shielding materials or even construction supports, it is possible to define own material using data tables. One can define chemical elements by setting their Z and atomic weight, even with a possibility of construction from different isotopes. Furthermore, a compound or molecule can be constructed by using density and elements, with their mass fraction, respectively relative counts.

solid

Goal of the method is to define size and shape for the object. The shapes that can be set are predefined, ranging from simple designs (box, sphere, ...), throughout more complicated ones (torus, parallelepiped, ...), up to boolean ones (intersections, subtractions and unions of any of the previous).

Size of the object is defined according to the volume type, though usually defined as the half length of the side.

logical

The role of the logical volume is to manage possible physical properties. It is built upon the solid object, adding information about material and sensitivity (ability to log data).

physical

Lastly, the object is placed inside the world volume with respect to its center, referring the logical volume object. This separation enables to use single logical volume for multiple repetitive insertions – such as pixels in pixel detector.

5.2.4 Particle Sources

The generation of particles in GEANT4 is done by either a particle gun or general particle source. They both enable choosing any type of known particles and setting their energies, orientations.

particle gun

Gun is a simple implementation of a particle point source, defined before the compilation of the code. User defines any desired randomization i.e. position relative to the center of the world volume, energies, directions even particle types.

This method is optimal for a more complex situation for a cost of developing more complicated algorithm.

general particle source

One of the main advantages of General Particle Source (GPS) is simple definition of particles and energies in a macro – without the need to recompile or reinitialize the code instance.

Furthermore, GPS can automatically generate and randomize particles according to set of predefined commands. This includes source types (point, plane, beam, surface and volume), shapes (simple 2D and 3D, in correspondence to the source type), direction and angular distribution, and energy spectra.

5.3 Tokamak COMPASS simulation

In order to better understand the response of Medipix2 detector in the tokamak environment, a simulation of the whole experimental setup had to be made.

The relatively simple construction of the detector allows for the manual definition, relying on repetition of pixels. However, it would not be practically possible to model the complex structure of the tokamak with the best possible precision therefore a way of conversion from Computer-Aided Design (CAD) model had to be found and utilized.

Techniques mentioned in the previous sections were utilized in order to simulate interaction of RE with the simple model. The proposed simulation is focused on the angular dependancy of RE interaction with material. Different values such as creation of secondary particles or deposition of energy were

monitored, furthermore, a response of the simulated Medipix2 detector was monitored.

In principle, this model could be used for any other particle transportation related processes – deposition of energy to different structures, production and transport of X-rays or neutrons and response of other existing particle diagnostic system.

5.3.1 Construction of model

The simulation model consists of Medipix2 detector and a simple model of the tokamak COMPASS. Due to the orientation of the detector, only dead layers, sensor and were simulated, not the whole PCB. Since the simulation was a proof-of-concept, the tokamak consists only of a limiter and vacuum chamber. However, in future the model should be expanded by additional parts such as coils or support structures.

Medipix2 detector

The model of Medipix2 detector was based on the previous work of author of this thesis. The former model was improved by using single logical volume and cloning of the individual pixels, instead of creating all 512×512 pixels as both logical and physical volumes. It enabled for easier data processing and memory consumption of the simulation.

The model is illustrated in in figure 5.3, with detailed description of all used materials and sizes.

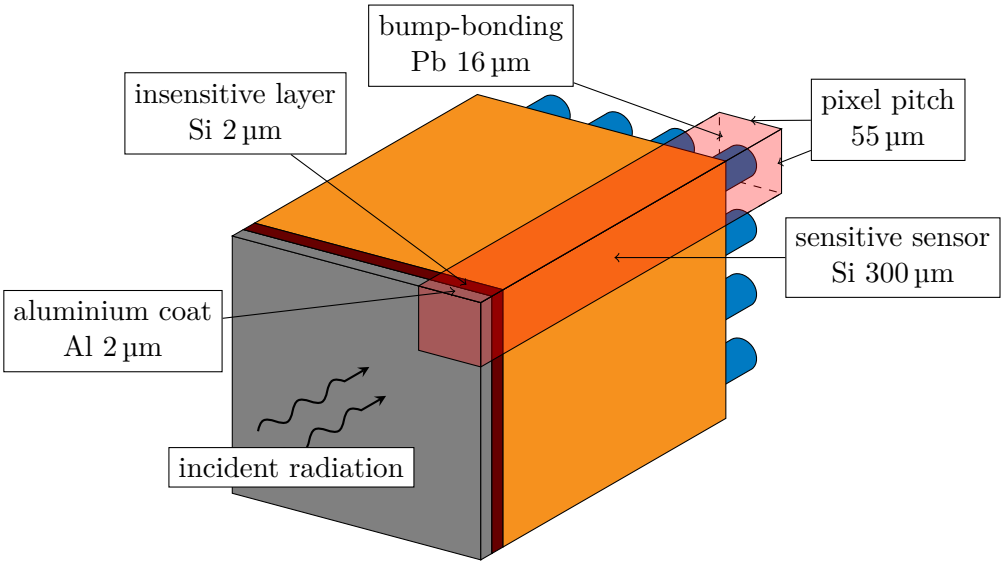

Figure 5.3: Illustration of Medipix2 detector model with a higlighted pixel. In the simulation, model consisted of 512×512 pixels instead of 4×4 as illustrated. An ideal direction (perpendicular to the surface) of the incident radiation is sketched.

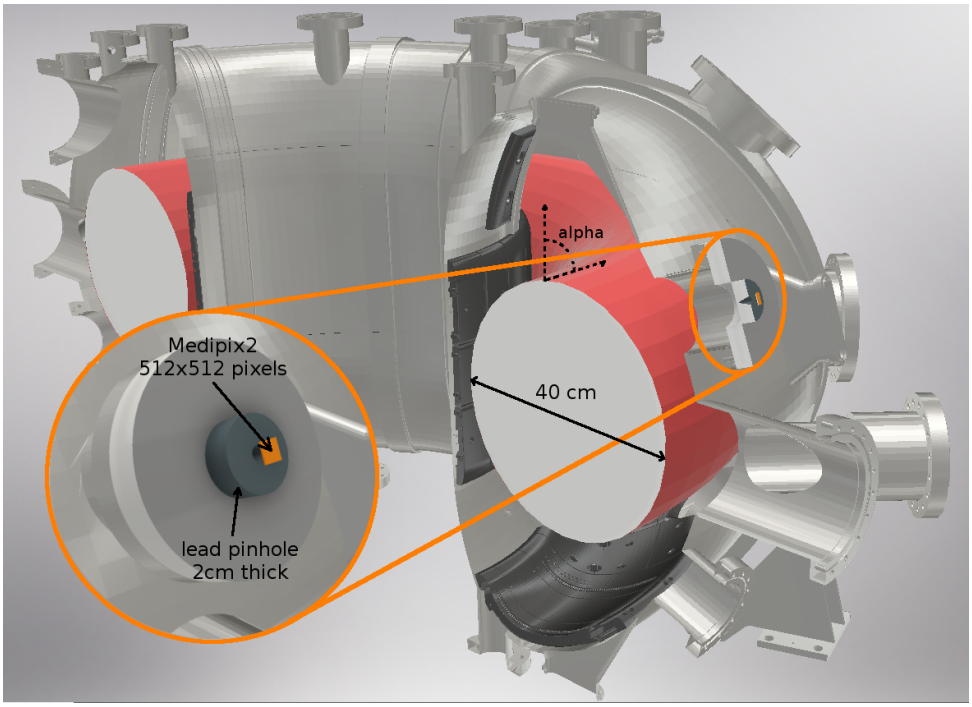

Figure 5.4: 3D model of vacuum chamber (steel inconnel 625), limiter (graphite R8650) and Medipix2 attached to the port with lead pinhole. Plasma with circular cross-section is illustrated with variable direction of particles α, in respect to the toroidal direction φ.

tokamak COMPASS

A set of stereolithography (stl) files of the vacuum chamber and limiter was provided by IPP ASCR by exporting from already existing CAD files. Afterwards a conversion using CAD to GEANT4 converter tool [1] was made in order to obtain a GDML model.

Two limiter and two chamber files were provided, varying in size – depending on the precision of the model. In the end, the larger files for both objects were used, the smaller being incompatible, having their volumes overlap. As the models were more precise, the requirements on computer memory and model initialization time were enormous (approximately 5 GB of RAM and tens of minutes of processor time).

The whole model is illustrated in figure 5.4, containing both limiter and vacuum chamber and material description. where both tokamak and detector with geometric optics were placed, was created out of vacuum.

5.3.2 Particle Generation

Since the simulation is focused on the angular dependency of RE, a source that generates particles on the surface of the torus with chosen angle had

[1] `https://github.com/tihonav/cad-to-geant4-converter` by Andrii Tykhonov, MIT license 2018

to be developed. For this purpose, a particle gun randomly position on a toroidal region has been utilized.

Toroidal randomization

The toroidal angle φ may be chosen uniformly from 0 to 2π, having point density f

$$f(\varphi) = \frac{1}{2\pi}. \tag{5.1}$$

However, if the poloidal angle θ also had uniform distribution for values from 0 to 2π, the point density would be higher inside the torus. Using transformation to toroidal coordinates, the required point density therefore is

$$f(\theta) = \frac{R_0 + r\cos\theta}{2\pi R_0}, \tag{5.2}$$

variables r and R_0 being radius, respectively major radius of torus.

As such cumulative distribution function for θ does not have closed-form inverse, the value can be obtained using rejection sampling. Values for θ and φ are uniformly distributed from 0 to 2π and an additional constraint is given using third uniformly distributed value x from 0 to 1. The constraint is given by

$$x \leq \frac{R_0 + r\cos\theta}{R_0 + r}, \tag{5.3}$$

where if true, the resulting point is generated on the surface of the torus, represented in Cartesian system (x, y, z) as:

$$\begin{bmatrix} (R_0 + r\cos\theta)\cos\varphi \\ (R_0 + r\cos\theta)\sin\varphi \\ r\sin\theta \end{bmatrix} \tag{5.4}$$

Otherwise a new randomization for all three variables θ, φ and x occurs.

The positions of particle gun were computed using (5.4) with R_0 being major radius at tokamak COMPASS and r its minor radius, thus simulating particles from the surface of the plasma.

Angular dependency

To model the angular dependency, a change of the direction of the radiation had to be applied uniformly for all particle guns, ensuring the same direction in respect to the surface of the torus. To achieve this a rotational transformation of the following form was applied:

$$\begin{bmatrix} \cos\varphi & -\sin\varphi & 0 \\ \sin\varphi & \cos\varphi & 0 \\ 0 & 0 & 1 \end{bmatrix} \cdot \begin{bmatrix} \cos\theta\cos\alpha \\ \sin\alpha \\ \sin\theta\cos\alpha \end{bmatrix} = \begin{bmatrix} \cos\theta\cos\alpha\cos\varphi - \sin\alpha\sin\varphi \\ \cos\theta\cos\alpha\sin\varphi + \sin\alpha\cos\varphi \\ \sin\theta\cos\alpha \end{bmatrix} \tag{5.5}$$

This ensures rotation of a radiation direction by a given angle α, in respect to the toroidal direction φ. For $\alpha \equiv 0\,\text{deg}$, the direction is perpendicular to

the surface of the torus, whereas for $\alpha \equiv 90\,\text{deg}$, particles follow the toroidal angle φ in any given point. This is illustrated in figure 5.4.

The transformation could be further enhanced by applying another rotation, giving an angle β which would define direction in respect to the poloidal direction θ. This, however, was not part of proposed simulation.

5.3.3 Sensitive region

To simulate the response of the detector, its logical volume was set as sensitive. This enabled acquisition of deposited energy and number of interactions from all of its pixels.

Since the geometry of the tokamak is represented as a single volume, distinguishing only different imported parts such as whole chamber or limiter, setting them as a sensitive volume would not yield interesting results. This was solved by the usage of a scoring mesh – a cube of $100 \times 100 \times 100$ voxels, cotaining the whole tokamak. Using such scorer enables detection of number of chosen attributes in each voxel, obtaining deposited energy, generation of secondary particles and even flux of all particles.

In addition to these a more precise and computation intensive process was set, acquiring data from each step of a particle track. It enables getting the energy and type of each individual particle within the whole simulated volume.

Chapter 6

Results

In this chapter, results from Medipix measurements and Geant4 simulations are presented.

Prior to all measurements, the detector has to be equalized in order to ensure equal response of all pixels to the incoming signal. The procedure was run on each detector used, using corresponding software discussed in previous chapters.

6.1 GOLEM

The main purpose of the measurements at tokamak GOLEM was to test the capabilities of Medipix2 to detect ionizing radiation during discharge which is usually detected by scintillator detectors. A simple setup was constructed with lead pinhole as geometric optics and positioned close to the tokamak, shown in the figure 6.1.

Different positions were tested, all with similar results. When the tokamak was in the regime for RE generation (according to [36]), Medipix2 detected radiation, even though it was placed behind the thick lead glass plate. Results are in figure 6.3.

One of issues at GOLEM was detector acquisition frequency. As the maximal frame rate for Medipix2 is 100 Hz, during the standard tokamak shot (lasting 20 ms) up to 2 frames could be made, with acquisition window of only 1 ms. However, the results indicate that semiconductor detectors are able to capture secondary radiation field and such diagnostics could be successfully used for the detection and measurements of the RE disruptions.

6.2 COMPASS

Medipix2 was part of the instrumentation for two RE campaigns at tokamak COMPASS. Since the typical discharge lasts hundreds of milliseconds, maximal acquisition rate of the detector was necessary in order to monitor temporal development of RE. For this purpose, the first campaign was mainly used for testing the newly developed CoaXPress readout and ASPIRE software. In order to obtain higher spatial resolution, a quad setup (combination

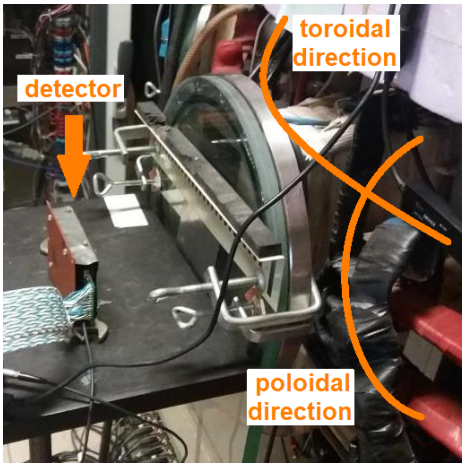

Figure 6.1: Detector setup at tokamak GOLEM.

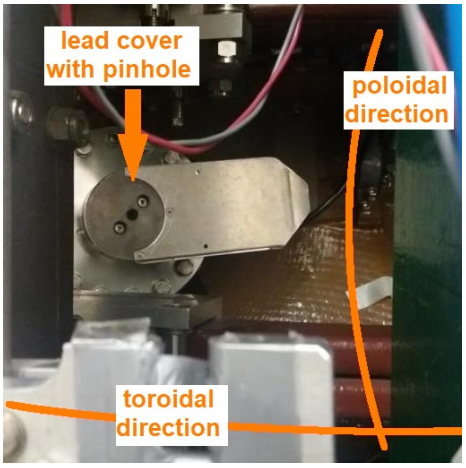

Figure 6.2: Pinhole setup at tokamak COMPASS.

of four chips) was used.

The detector was attached to a 2 cm thick lead pinhole, connected to a side port at tokamak, see figure 6.2. The port was covered with a beryllium window, which together with pinhole, provide geometrical optics system with sufficient resolution of a part of the inner side of the vacuum vessel.

Acquisition was triggered, however, the trigger source was frequently changed in between the shots due to problems related to the signal receiving. It was finally resolved by using a trigger repetition, sending 10 signals during 1 ms.

6.2.1 Campaign 1

The first RE campaing with the usage of Medipix2 detector and CoaXPress readout was at the end of 2016 - 9th to 20th of December.

Position of the detector, together with other diagnostic types, is shown in the figure 1a in the appendix. Due to the positioning, the detector was unable to obtain any data showing spatially-relevant information, which could be caused by non-ideal orientation in respect to the vacuum vessel.

The results from a couple of successful shots are in figures 6.4a, 6.4b (more data in appendix figure 2), where histograms from Medipix2 are compared to X-ray data from a HXR and neutron scintillator detector. A typical information of a tokamak state – plasma density n_p, current I_p, loop voltage U_loop as well as H-α emission is provided. The data analysis showed promising results in the respect of correlation of Medipix2 data and acquired X-ray intensities, as well as flux of photo-neutrons during the end of the discharge.

It was also found that such high energies of incident X-rays and gamma rays produce high number of scattered electrons from the pinhole, which were observed in the detector. Therefore additional aluminium shielding was added for the purposes of the next campaign to reach electron equilibrium due to the similar proton numbers of silicon and aluminum

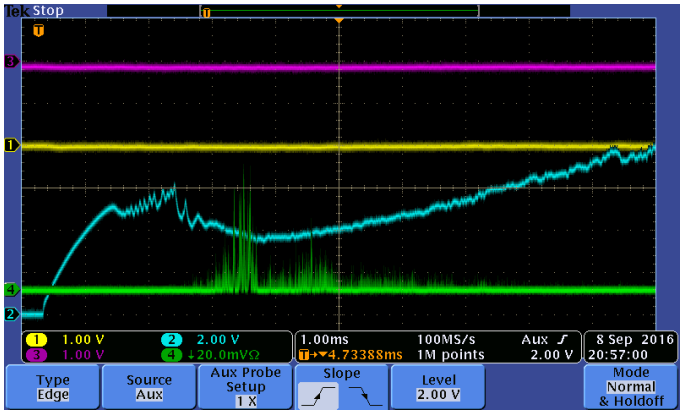

(a) : Oscilloscope signal, channel 4 represents scintillator - signal corresponds to HXR generated by RE.

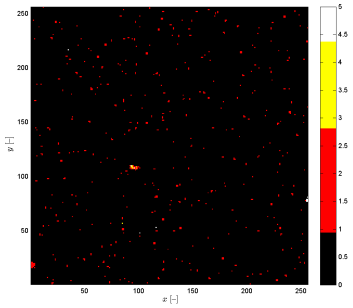

(b) : Medipix2 data, taken during discharge.

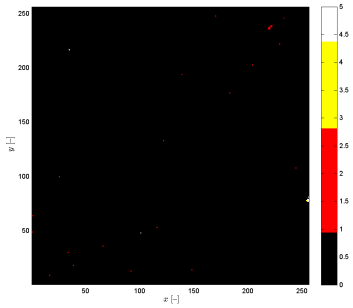

(c) : Medipix2 data, taken after discharge.

Figure 6.3: Data from GOLEM discharge 22207. Medipix2 (covered by lead pinhole) had acquisition time set to 10 s in order for the detector to be sensitive during discharge. Empty frame right after the discharge for comparison, together with data from scintillator.

6.2.2 Campaign 2

The second campaing with Medipix2 and CoaXPress readout was held between 12th to 23rd of June 2017.

Position of the detector, together with other diagnostic types, is shown in the figure 1b in the appendix. The CAD image of the used port is in the figure 6.5, using the same configuration as in the previous campaign - only with addition of aluminium foil and additional shielding all around the detector setup. As is clearly visible from the figures, geometric configuration was chosen in order to observe part of the HFS limiter.

Similarly to the previous experiments, an analysis of temporal evolution of signal from Medipix2, scintillator and photo–neutron counter was made. The sum of the pixelated semiconductor detector signal is comparable to other diagnostics in most of the shots. The offsets could be caused by wrong stating of the trigger time during the analysis. Some of the results are shown in figures 6.4c and 6.4d, remaining plots are in the appendix figure 3.

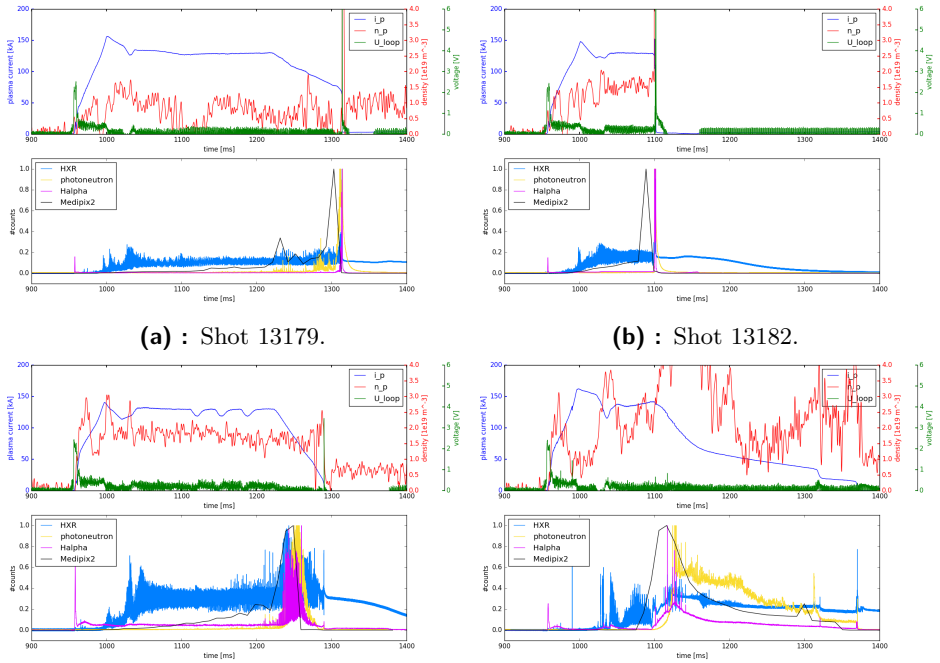

(a) : Shot 13179.

(b) : Shot 13182.

(c) : Shot 14513.

(d) : Shot 14599.

Figure 6.4: Upper figures represent typical discharge parameters – plasma density n_p, current I_p and loop voltage U_loop. Lower figures show time development of X-ray flux measured by Medipix2, scintillator and photo-neutron counter as well as H-α emission. Time stamping of the Medipix2 is 10.2 ms (1 ms acquisition and 9.2 ms dead time). Datasets are normalized to the maximal value.

In addition to previous measurements, experiments with vertical positioning of the plasma column were performed. Example of preset shaper is in figure 6.6d, compared to the images obtained from the detector in figures 6.6a to 6.6c. A larger signal in a form of a cluster is visible, changing its position with the time. Data from the y–axis histograms and of the frames show change of the position of about 30 pixels during 20.4 ms, corresponding to couple centimeters of plasma position. Moreover a spatial dependency of a signal is visible in a form of a slope in histograms – higher values on the left side for x-axis, however a constant signal is detected for y-axis. This height of the slope also changes in time as for the first frame 6.6a, the difference between two sides is only about 30 hits (from 40 to 10), for the last frame 6.6c it is about 90 (from 115 to 25). The higher rate is on the same side as is the direction of incoming RE, and could be caused by scattering of X-rays from the magnets and vacuum chamber.

During one of the last discharges, an interesting time-development of a spatial signal was observed, shown in appendix figure 4. The effect can be monitored in the lower left part of the quad detector, in which a clear change of the signal is visible. Since the interpretation of such effect is not possible without fully understanding the geometry, where RE produced secondary radiation, GEANT4 simulation of the tokamak is a necessity for data analysis

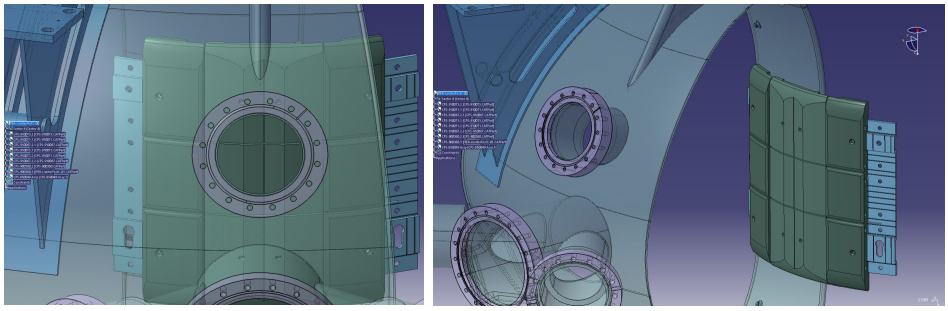

(a) : Perpendicular view to the port. **(b) :** Side view of the setup.

Figure 6.5: CAD model of used port during second COMPASS campaign. Distance between the attached pinhole to the upper port is 50 cm, distance between the pinhole and the detector is 0.5 cm.

and interpretation. The GEANT4 simulation can be also used to optimize the shielding and geometrical optics of the X-ray camera. This is important because of the Compton electrons generated in the shielding, which are easily detected by the detector, which is in sharp contrast with low detection efficiency of high energy X-ray and gamma photons in the silicon sensor. So far, the only viable statement is that the signal is not a detector defect, as the hit-rate reaches less than 10 % of the maximal value and does not show typical effects of the lost configuration of the detector – no noise visible after the end of discharge.

6.2.3 Simulation of COMPASS in Geant4

Setup

The performed simulation of RE interaction was done using electrons spatially distributed over a surface of torus according to the equation (5.4). The region of interest was around the Medipix2 detector, modeled in the same position as was its placement in the second COMPASS RE campaign ($\varphi \equiv 0°$ and $\theta \approx 30°$). Therefore, the random generation was made for toroidal angle φ from $-45°$ to $22.5°$ and for poloidal angle θ from $-22.5°$ to $60°$.

Major radius of simulated torus R_0 was set to 56 cm and minor radius to 20 cm, in accordance to tokamak COMPASS. Spatial distribution of all vertices is visualized in appendix in figure 8 for planes XY, YZ and XZ in Cartesian coordinates.

Energies of generated electrons were uniformly distributed from $1 \cdot 10^{-3}$ MeV to 10 MeV, plot of the distribution is in appendix in figure 9.

To monitor angular dependency of the detector response, the simulation was run for different settings of the angle α – characterizing deviation of the direction perpendicular to the surface towards the toroidal direction. The direction of simulated RE was calculated using equation (5.5), for α from $0°$ to $90°$ with step of $10°$. Each one of 10 performed simulations consisted of 1.1M generated particles.

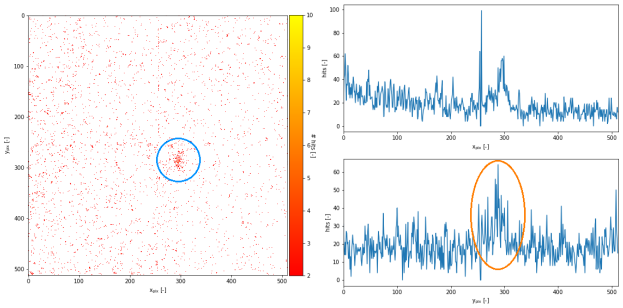

(a) : $t = 1014.0\,\text{ms}$.

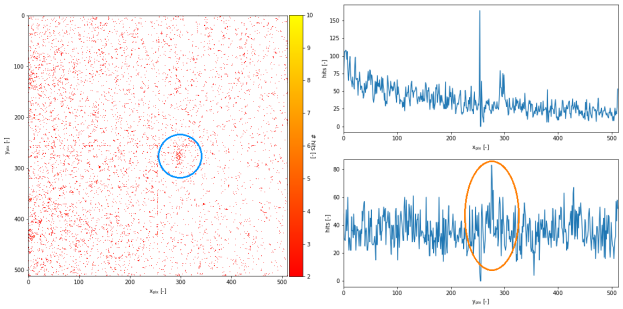

(b) : $t = 1024.2\,\text{ms}$.

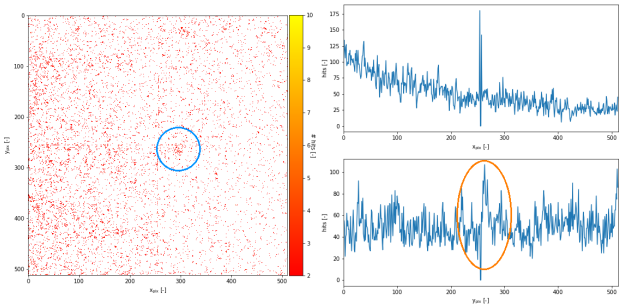

(c) : $t = 1034.4\,\text{ms}$.

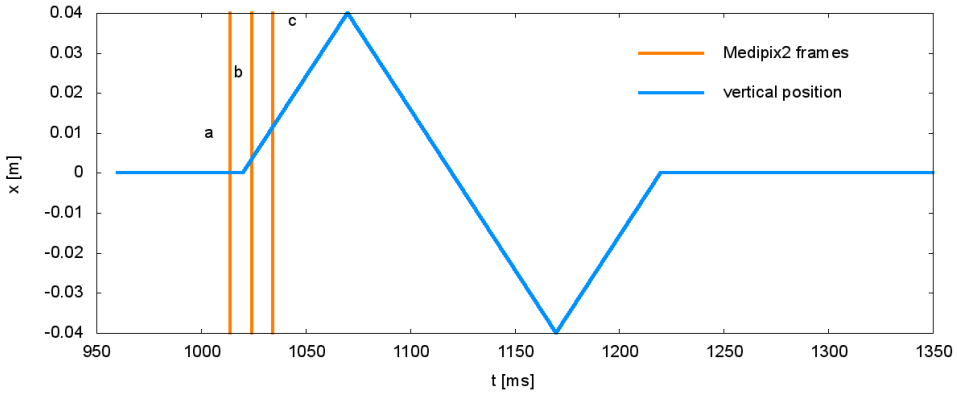

(d) : Vertical shaping of the plasma, lines representing Medipix2 frames.

Figure 6.6: Data from Medipix2 during shot 14555 at tokamak COMPASS. Masked hit values above 10 and below 2. Visible positioning of plasma on limiter is observed on y–axis (from pixel 300 in upper figure, to 270 in lower figure, during 20.4 ms), comparable to preset vertical shaper shown in bottom figure. Moreover, a spatial dependency of signal is clear, as x–axis shows a clear slope whereas y–axis is constant.

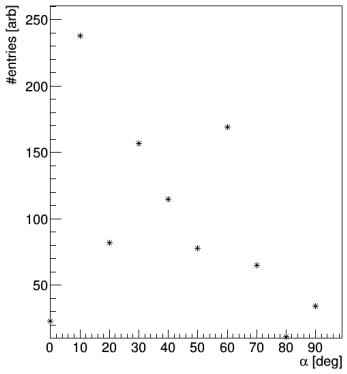

(a) : Hits in Medipix2 model.

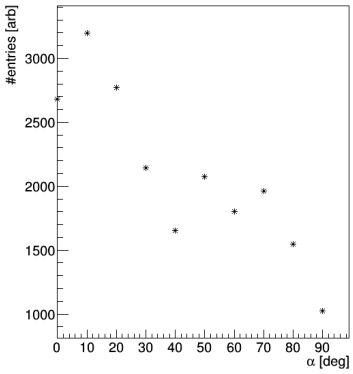

(b) : Number of non-interacting photons in Medipix2 model.

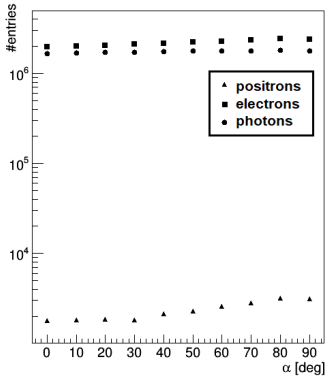

(c) : Total number of generated secondary particles.

Figure 6.7: Angular dependency of different parameters.

Results

Counts of Medipix2 hits and non-interacting photons passing through the detector, as well as total number of generated secondary particles against the value of angle α are plotted in figure 6.7. The number of detector hits does not correspond to the amount measured by the detector during campaigns, due to different flux of RE presented in tokamak and simulation.

The observed decrease of hits measured by Medipix2 could be caused by the fact that for large angles, the detector was not in line with the direction of primary electrons. On the other hand, increased numbers of generated secondary particles could be a consequence of a shift of interaction points of RE and material to a different part of the vacuum chamber. To better characterize this dependency a simulation of particles from the whole surface of the plasma torus would be necessary.

Furthermore, a spatial and spectral analysis of primary and secondary particles was performed.

In order to reduce the time needed for the processing of the simulation,

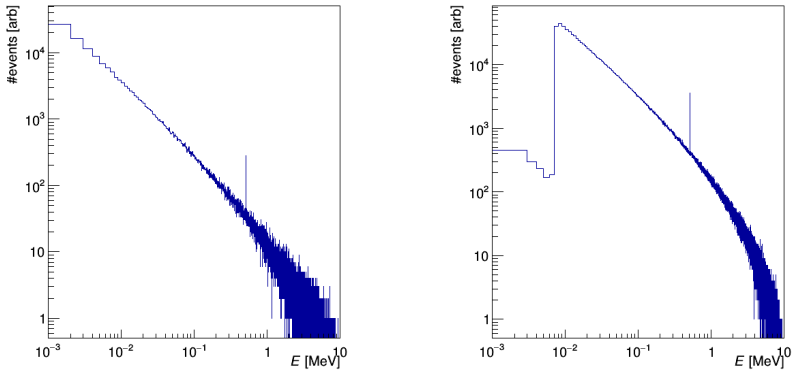

(a) : No production cut (≡ 1 keV in all materials).

(b) : Production cut 100 µm (≈ 7 keV in steel of vacuum chamber).

Figure 6.8: Comparison of energy distributions of secondary photons for different values of production cuts. In both plots a sharp peak corresponding to the annihilation of positrons ($E = 511\,\mathrm{keV}$) is visible. Runs were simulated with different number of events (left 100k, right 1.1M)

a production cut for secondary particles was set – 200 µm for electrons and 100 µm for photons. These values correspond to ≈ 390 keV and ≈ 7 keV in steel of the vacuum chamber, respectively. All of the simulations were performed using these cuts as it improved the speed of computations by more than 100 %. Moreover, the setting did not have a considerable impact on the generation of the particles detectable by the model of the Medipix2 detector.

Energy distribution of secondary photons is in figure 6.8, compared for run with and without defined production cut. The energy cut is seen as a steep decrease in number of secondary particles – similar in shape to the absorption edge. Nevertheless, both plots show a sharp peak corresponding to the annihilation energy of positrons ($E = 511\,\mathrm{keV}$) and have similar distribution.

More energy distributions of secondary particles are plotted in figure 6, their radial energy profiles in 7. The profile corresponds to the instantaneous energy of specified particles in each point in space, dependent on distance r from the centre of the simulated tokamak. Energy profile of primary particles is in figure 6.9. The confinement of the RE inside the torus is visible, only a small number of particles penetrate limiter (≈ 330 mm) and most of the highly energetic electrons lose their energy on the LFS side of the chamber (≈ 790 mm). The profiles of the secondary particles are similar.

Positions and tracks of primary electrons and all secondary particles in XY plane are plotted in figure 6.10. The plots show spatial distribution of positions of generation of particles (vertices), accompanied by their integrated tracks in space (weighted using their instantaneous kinetic energy). The integrated tracks therefore correspond to the amount of energy being present in each point in space, combined for all specified particles. Plots of tracks for different angles α for both primary and secondary particles are in appendix in figures 10 and 12 with their respective spatial distributions of vertices in

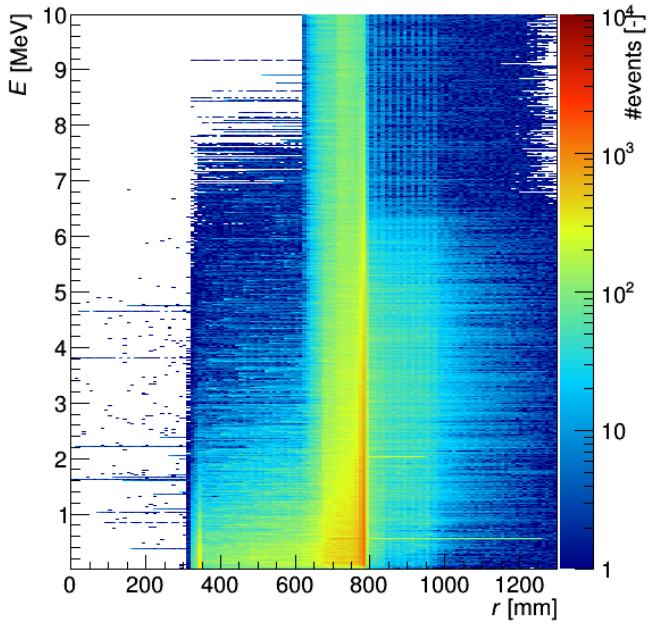

Figure 6.9: Radial energy profile of primary particles. The values correspond to the instantaneous energy of primary particles in each point in space, dependent on distance r from the centre of the torus.

figures 8 and 11. The plots are for visualization in XY plane, plots in other planes (YZ and XZ) in the following figures.

The position of interaction of RE and vacuum chamber is shifted according to the angle α. Deposition of energy is highest in the interaction points – they correlate to the position of verticis of secondary particles, as well as energy loss visible from the integrated tracks. Different parts of the chamber are visible as a simple outline caused by higher number of interactions in the material.

It may be also observed that trajectories of secondary photons are mostly keeping the direction of the primary electrons, however, both primary and secondary electrons, as well as secondary positrons, deviate a lot. This is caused by the small mass attenuation coefficient for high energy photons and easy scattering of electrons and positrons in the material.

The model was successfully tested and may be easily adapted for other experiments. To further improve the simulation of the RE interaction processes, the spatial and spectral distribution of the primary electrons should be implemented from specialized computational models, which simulate the process of generation and transportation of RE in plasma.

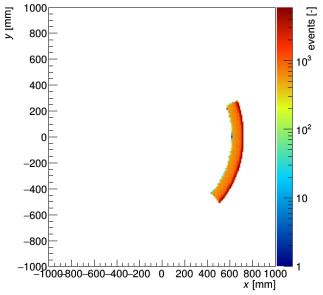

(a) : Vertices of primary electrons.

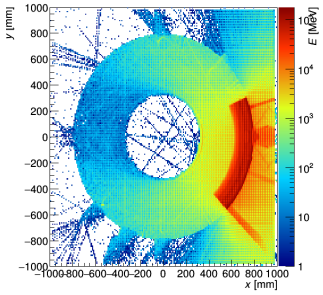

(b) : Integrated tracks of primary electrons.

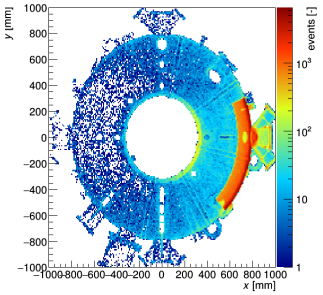

(c) : Vertices of secondary electrons.

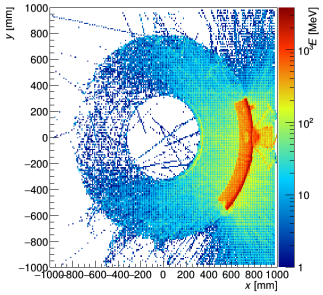

(d) : Integrated tracks of secondary electrons.

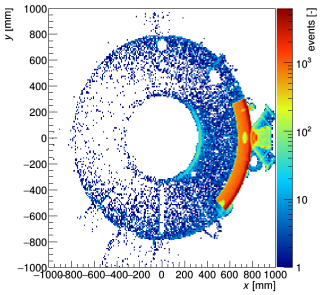

(e) : Vertices of secondary photons.

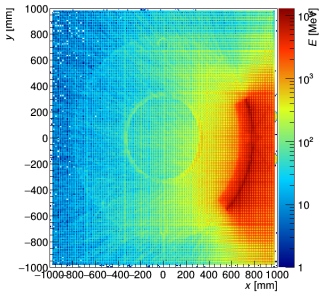

(f) : Integrated tracks of secondary photons.

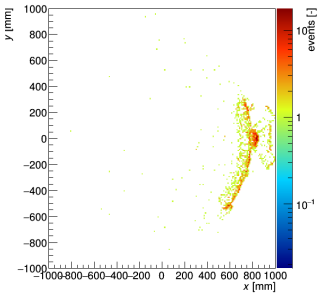

(g) : Vertices of secondary positrons.

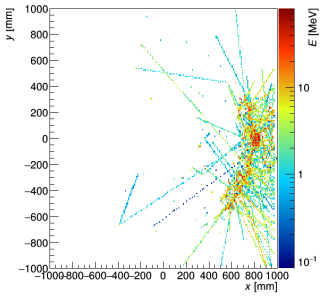

(h) : Integrated tracks of secondary positrons.

Figure 6.10: Spatial distribution of vertices (positions of generation) and tracks of secondary particles in XY plane. Tracks are integrated in space, weighted by the instantaneous energy of the particle. Primary particles were generated for angle $\alpha = 0°$.

Chapter 7

Conclusions

Semiconductor pixel detectors were demonstrated to be a functional new addition to the RE diagnostic methods at tokamaks. Recorded secondary photon hit data correlate well with other used diagnostic methods. Since the full potential of semiconductor pixel detectors in this field of research is not yet fully exploited, their application should be studied further. A novel segmented semiconductor detection system could be developed as a new method of diagnostics, providing both spatial and temporal resolution throughout the plasma discharge.

Proper operation of the Medipix2 detector with a newly developed CoaX-Press readout system and software ASPIRE has been tested successfully. The time development of the photon flux in the acquired data is consistent with the existing X-ray diagnostics instruments at the COMPASS tokamak. In addition, the pixelated detector proved to be able to extract spatial information using geometrical optics. However, as the photon flux was large and the energy distribution of the radiation was focused on the hard part of the X–ray spectrum, only some of the acquired frames contained relevant information.

For all studied devices, higher frame-rate in the order of kHz could be a major improvement to the measurement, as more precise data would be obtained. Moreover, for the RE, studies a direct measurements of the electrons in the chamber would be useful, as the detectors are better suited to detect directly ionizing particles.

Due to the nontrivial interpretation of the measured data, a Geant4 simulation model of the COMPASS tokamak system was developed. Similar Monte Carlo models are typically deployed for all large high energy physics experiments in order to simulate transport and interaction of ionizing radiation.

The simulation developed in this work is a proof of concept, only a vacuum chamber and a limiter are included in the model, eventually to be expanded with other tokamak components. Nevertheless, the preliminary results show outstanding performance, giving tracks and energies of primary and secondary particles. Such simulation model has not been implemented previously at the COMPASS tokamak.

For the studies of RE, the simulated electrons should be defined more accurately in both spatial and spectral region using results from specialized computational models of generation and transport of RE. Furthermore, a

simulation of other RE relevant diagnostics systems should be implemented. Since the execution of the GEANT4 physics models is computationally demanding, its execution could be accelerated by modifying the code to support parallel event processing using either multiple CPU cores or even better optimized graphical processing units available in modern personal computers.

In principle, this model could be used for study of any other particle transport related processes – deposition of energy to tokamak structures, transport of X-rays or generation of photoneutrons and modeling the response of any other particle diagnostic system. Such model could be also utilized for the survey of radiation safety of the area, an important factor for the COMPASS-upgrade.

Bibliography

[1] JET/UKAEA, "Generating runaway electrons in JET to benefit ITER," 10 2015. https://www.euro-fusion.org/2015/06/generating-runaway-electrons-in-jet-to-benefit-iter/.

[2] J. Lawson, "Some criteria for a power producing thermonuclear reactor," tech. rep., Atomic Energy Research Establishment, 12 1955. Technical Report.

[3] J. Wesson and D. Campbell, *Tokamaks*. Oxford university press, 4 ed., 2011, ISBN: 0199592233.

[4] J. Connor, A. Kirk, and H. Wilson, "Edge localised modes (ELMs): Experiments and theory," *AIP*, vol. 1013, 05 2008, http://dx.doi.org/10.1063/1.2939030.

[5] J. Zajac *et al.*, "Power supply system for the COMPASS tokamak reinstalled at the IPP, prague," *Fusion Engineering and Design*, vol. 84, pp. 2020–2024, 06 2009, http://dx.doi.org/10.1016/j.fusengdes.2008.11.092.

[6] R. Panek *et al.*, "Status of the COMPASS tokamak and characterization of the first H-mode," *Plasma Phys. Control. Fusion*, vol. 58, 2016.

[7] R. Mitteau *et al.*, "Lifetime analysis of the ITER first wall under steady state and off normal load," *Physica Scripta*, vol. 2011, p. 7, 12 2011, http://arxiv.org/abs/http://stacks.iop.org/1402-4896/2011/i=T145/a=014081.

[8] C. Reux *et al.*, "Runaway beam studies during disruptions at JET-ILW," *Journal of Nuclear Materials*, vol. 463, pp. 143 – 149, 2015, http://dx.doi.org/10.1016/j.jnucmat.2014.10.002.

[9] G. Arnoux *et al.*, "Heat loads on plasma facing components during disruptions on JET," *Nuclear Fusion*, vol. 48, p. 8, 7 2009, http://dx.doi.org/10.1088/0029-5515/49/8/085038.

[10] D. D. Schnack, *Lectures in Magnetohydrodynamics*. Springer-Verlag Berlin and Heidelberg Gmbh & Co. Kg, 1 ed., 2009, ISBN: 9783642269219.

[11] H. Dreicer, "Electron and ion runaway in fully ionized gas i," *Physical Review*, vol. 115, no. 238, 1959, http://dx.doi.org/10.1029/2004GL019795.

[12] A. Stahl *et al.*, "Effective critical electric field for runaway-electron generation," *Physical Review Letters*, vol. 144, no. 11, 2015, http://dx.doi.org/10.1103/PhysRevLett.114.115002.

[13] O. Ficker, "Generace, ztraty a diagnostika ubihajicih elektronu v tokamacich," Master's thesis, FNSPE CTU in Prague, 2015.

[14] G. F. Knoll, *Radiation Detection and Measurement*. John Wiley & Sons, 4 ed., 2010, ISBN: 978-0-470-13148-0.

[15] M. J. Berger, "Monte carlo calculation of the penetration and diffusion of fast charged particles," *Meth. Comp. Phys*, vol. 1, pp. 135–215, 1963.

[16] B. Grosswendt, "The physics of particle transport: Electrons and photons," 1996. Training Course at Bologna.

[17] O. Klein and Y. Nishina, "Über die streuung von strahlung durch freie elektronen nach der neuen relativistischen quantendynamik von dirac," *Zeitschrift für Physik*, vol. 52, pp. 853–868, 11 1929, http://dx.doi.org/10.1007/BF01366453.

[18] S. Dietrich and B. Berman, "Atlas of photoneutron cross sections obtained with monoenergetic photons," *Atomic data and nuclear data tables*, vol. 38, pp. 199 – 338, 03 1988.

[19] M. Berger, J. Hubbell, S. Seltzer, J. Chang, J. Coursey, R. Sukumar, D. Zucker, and K. Olsen, "NIST standard reference database 8 (XGAM)," 11 2010. XCOM: Photon Cross Sections Database https://www.nist.gov/pml/xcom-photon-cross-sections-database.

[20] G. Lutz, *Semiconductor Radiation Detectors*. Springer-Verlag Berlin and Heidelberg, 01 2007, ISBN: 978-3-540-71679-2.

[21] B. Kolbinger, *Simulation of a Silicon-Strip Detector*. Institute of High Energy Physics, Torino, 11 2012. http://personalpages.to.infn.it/~cartigli/Weightfield2/Manual_files/Manual_Weightfield.pdf.

[22] W. Shockley, "Currents to conductors induced by a moving point charge," *Journal of Applied Physics*, vol. 9, pp. 635 – 636, 10 1938, http://dx.doi.org/10.1063/1.1710367.

[23] S. Ramo, *Currents Induced by Electron Motion*, vol. 27, IEEE, 09 1939.

[24] X. Llopart, *Design and characterization of 64K pixels chips working in single photon processing mode*. PhD thesis, Mid Sweden University, 2007.

[25] G. Neue, M. Hejtmanek, M. Marcisovsky, and P. Voles, "Flexible DAQ card for detector systems utilizing the CoaXPress communication standard," *Journal of Instrumentation*, vol. 10, p. 8, 04 2015, http://dx.doi.org/10.1088/1748-0221/10/04/C04013.

[26] P. **Svihra**, "Adapted software for pixel readout - ASPIRE user manual," 12 2016. TACR - FJFI-CK 2016/12.

[27] M. Hejtmanek, G. Neue, , and P. Voles, "Software interface for high-speed readout of particle detectors based on the CoaXPress communication standard," *Journal of Instrumentation*, vol. 10, p. 6, 04 2015, http://dx.doi.org/10.1088/1748-0221/10/06/C06011.

[28] X. Llopart *et al.*, "Timepix, a 65k programmable pixel readout chip for arrival time, energy and/or photon counting measurements," pp. 485–494, 2008, http://dx.doi.org/10.1016/j.nima.2007.08.079.

[29] B. van der Heijden *et al.*, "Spidr, a general-purpose readout system for pixel asics," *Journal of instrumentation*, vol. 12, 2017.

[30] A. Zhao, P. **Svihra**, *et al.*, "Coincidence velocity map imaging using tpx3cam, a time stamping optical camera with 1.5 ns timing resolution," *Review of Scientific Instruments*, vol. 88, 11 2017, http://scitation.aip.org/content/aip/journal/rsi/88/11/10.1063/1.4996888.

[31] A. Bielajew, "Fundamentals of the monte carlo method for neutral and charged particle transport." university lecture, 10 2001.

[32] T. Goorley *et al.*, "Initial MCNP6 release overview," *Nuclear Technology*, vol. 180, pp. 298 – 315, 12 2012.

[33] A. Ferrari, P. R. Sala, A. Fasso, and J. Ranft, "FLUKA: A multi-particle transport code (program version 2005)," 2005.

[34] T. Böhlen *et al.*, "The FLUKA code: Developments and challenges for high energy and medical applications," *Nuclear Data Sheets*, vol. 120, pp. 211 – 214, 2014, http://www.sciencedirect.com/science/article/pii/S0090375214005018.

[35] S. Agostinelli *et al.*, "Geant4: A simulation toolkit," *Nucl. Instrum. Meth.*, vol. A506, pp. 250–303, 2003, http://dx.doi.org/10.1016/S0168-9002(03)01368-8.

[36] O. Ficker *et al.*, "Tokamak GOLEM for fusion education - chapter 6," in *42nd EPS Conference on Plasma Physics*, 2015.

Medipix2 measurements

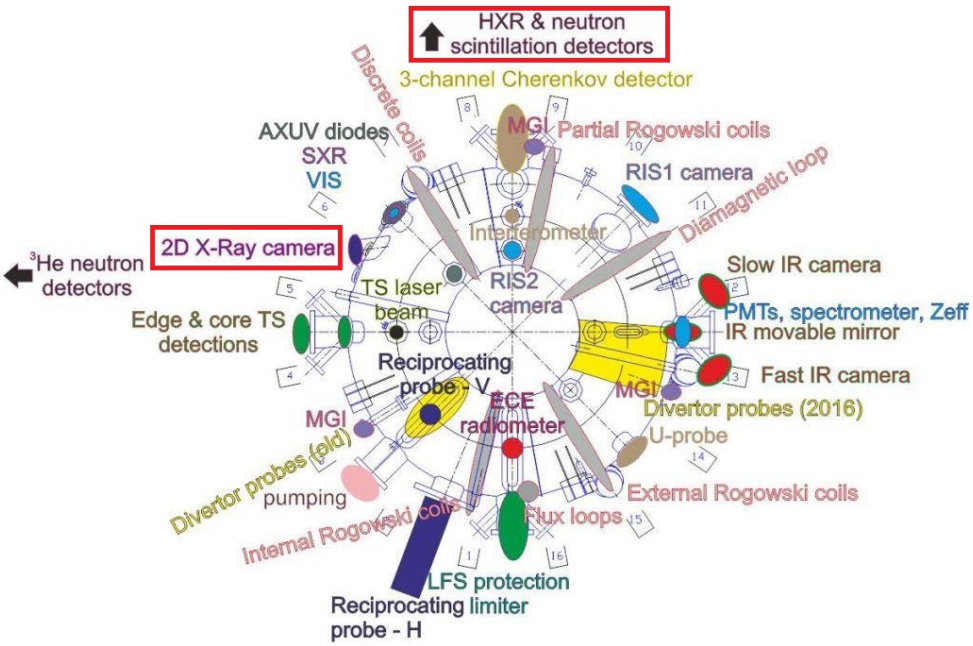

(a) : First campaign, Medipix2 on left side.

Figure 1: Types of diagnostics during both COMPASS RE campaign. Medipix2 is stated as a 2D X-ray camera.

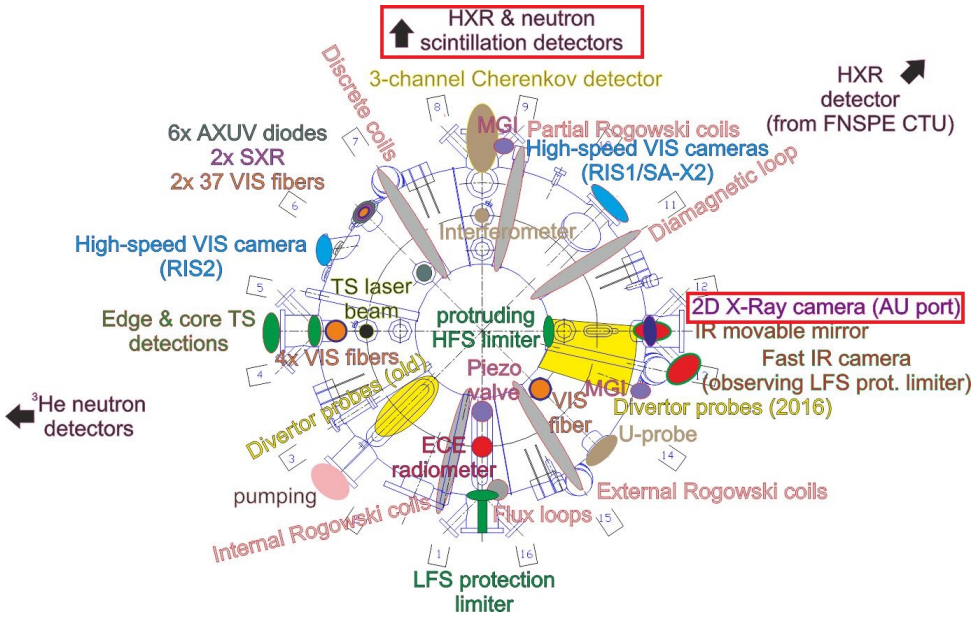

(b) : Second campaign, Medipix2 on right side.

Figure 1: Types of diagnostics during both COMPASS RE campaign. Medipix2 is stated as a 2D X-ray camera.

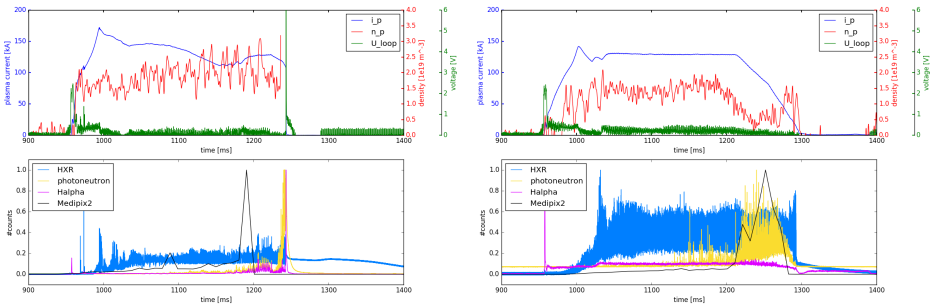

(a) : Shot 13091. **(b) :** Shot 13178.

Figure 2: Upper figures represent typical discharge parameters – plasma density n_p, current I_p and loop voltage U_loop. Lower figures show time development of X-ray flux measured by Medipix2, scintillator and photo-neutron counter as well as H-α emission. Time stamping of the Medipix2 is 10.2 ms (1 ms acquisition and 9.2 ms dead time). Datasets are normalized to the maximal value.

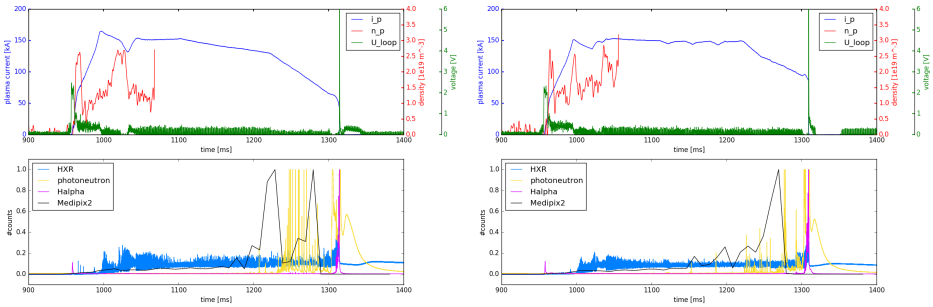

(a) : Shot 14494. **(b) :** Shot 14509.

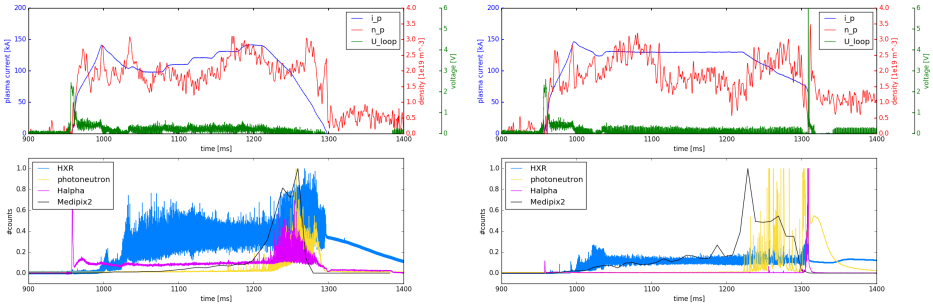

(c) : Shot 14517. **(d) :** Shot 14553.

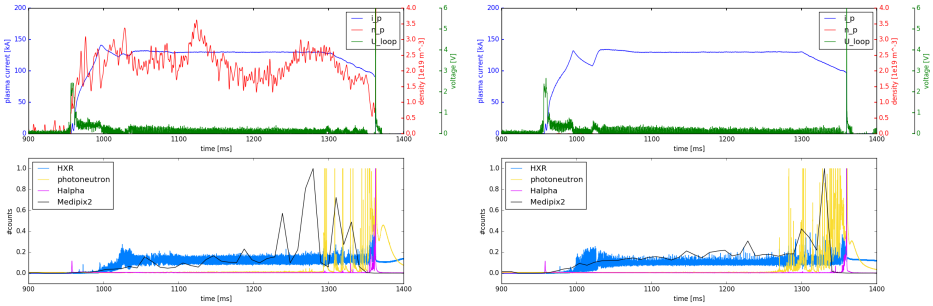

(e) : Shot 14554. **(f) :** Shot 14555.

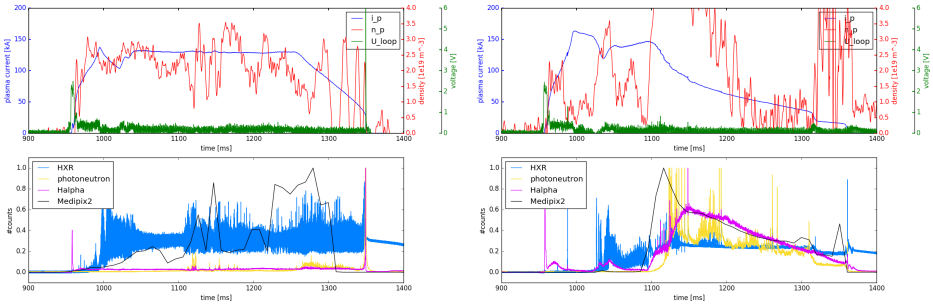

(g) : Shot 14557. **(h) :** Shot 14601.

Figure 3: Upper figures represent typical discharge parameters – plasma density n_p, current I_p and loop voltage U_loop. Lower figures show time development of X-ray flux measured by Medipix2, scintillator and photo-neutron counter as well as H-α emission. Time stamping of the Medipix2 is 10.2 ms (1 ms acquisition and 9.2 ms dead time). Datasets are normalized to the maximal value.

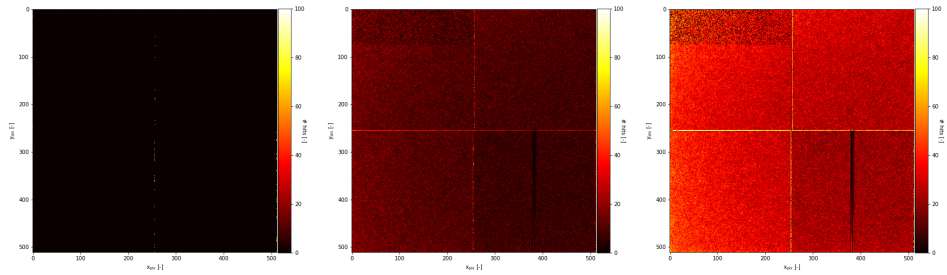

(a) : $t = 1075.2\,\text{ms}$. **(b) :** $t = 1085.4\,\text{ms}$. **(c) :** $t = 1095.6\,\text{ms}$.

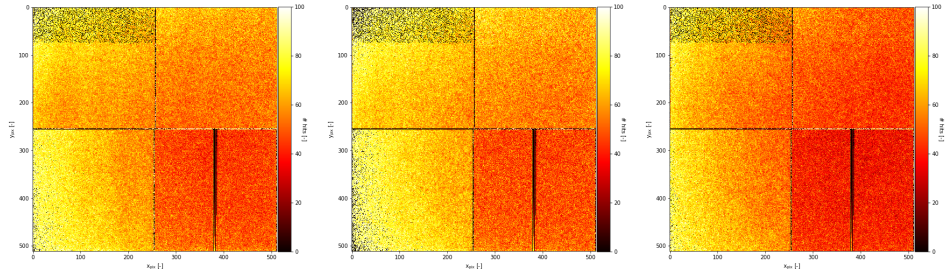

(d) : $t = 1105.8\,\text{ms}$. **(e) :** $t = 1116.0\,\text{ms}$. **(f) :** $t = 1126.2\,\text{ms}$.

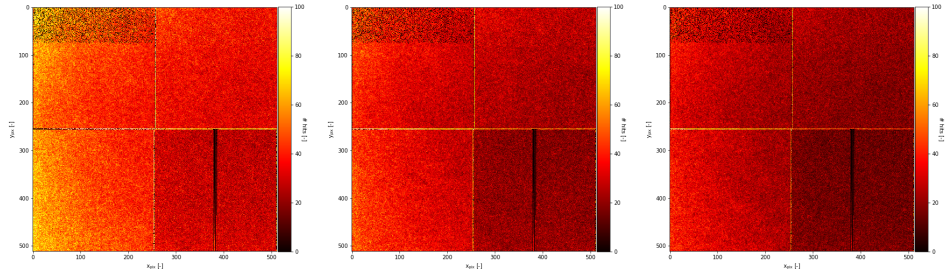

(g) : $t = 1136.4\,\text{ms}$. **(h) :** $t = 1146.6\,\text{ms}$. **(i) :** $t = 1156.8\,\text{ms}$.

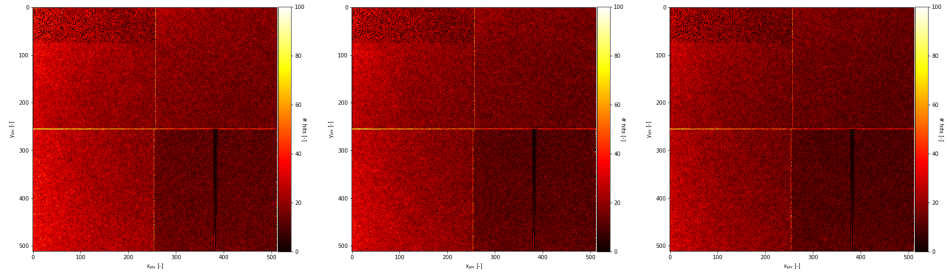

(j) : $t = 1167.0\,\text{ms}$. **(k) :** $t = 1177.2\,\text{ms}$. **(l) :** $t = 1187.4\,\text{ms}$.

Figure 4: Temporal development of signal from Medipix2 during shot 14599 shown in raw data. Visible change of spatial position of the signal in dependent on the time. Masked values above 100, part of upper left chip with bad configuration, THL in lower right part to different value.

Geant4 simulations

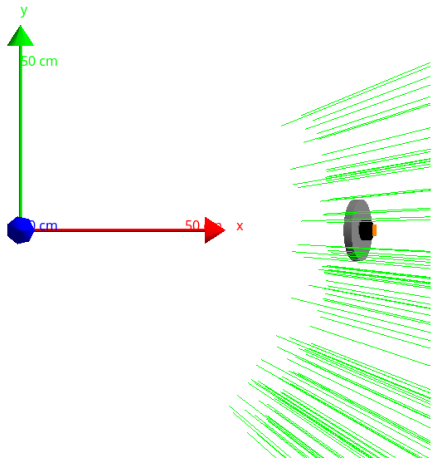

(a) : XY plane.

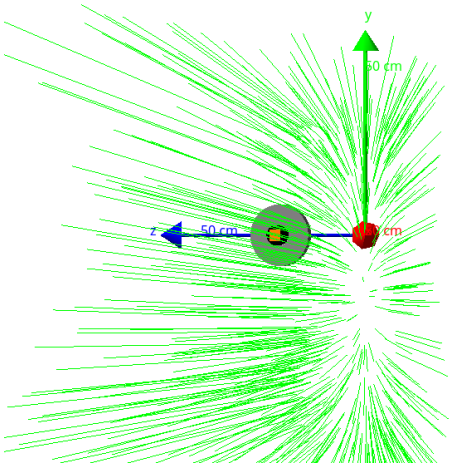

(b) : YZ plane.

Figure 5: Generation of primary particles. Visualized Medipix2 detector and lead pinhole. Axes represent 50 cms.

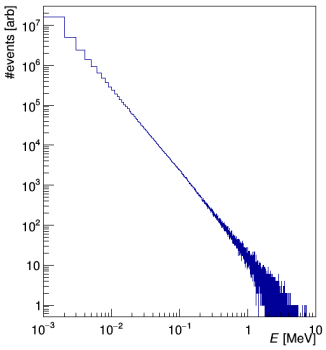

(a) : No production cut (≡ 1 keV in all materials), electrons.

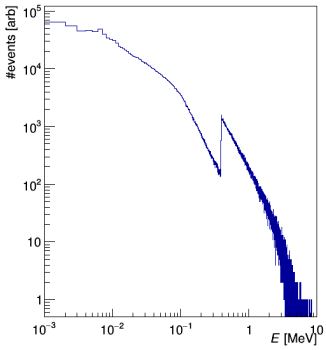

(b) : Production cut 200 µms (≈ 390 keV in steel of vacuum chamber) electrons.

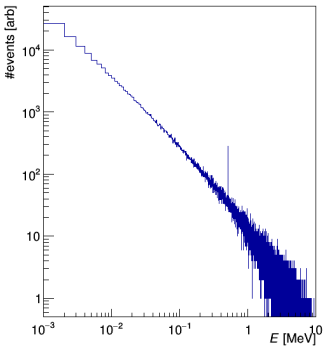

(c) : No production cut (≡ 1 keV in all materials), photons.

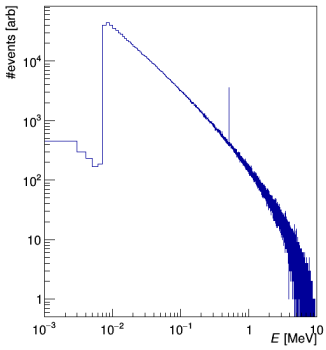

(d) : Production cut 100 µms (≈ 7 keV in steel of vacuum chamber) photons.

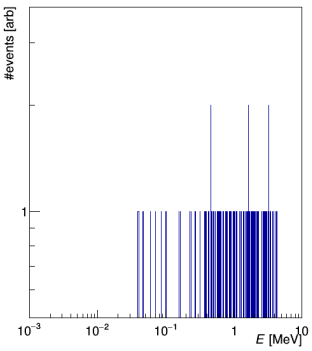

(e) : No production cut (≡ 1 keV in all materials), positrons.

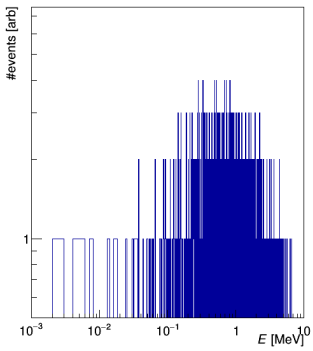

(f) : No production cut (≡ 1 keV in all materials), positrons.

Figure 6: Energy distributions of secondary particles. Left image represents run without production cut, right is using predefined cut 200 µm for electrons and 100 µm for photons (corresponding to ≈ 390 keV and ≈ 7 keV in steel of vacuum chamber, respectively). Runs were simulated with different number of events (left 100k, right 1.1M).

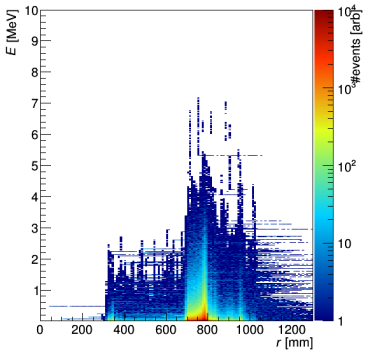

(a) : No production cut (≡ 1 keV in all materials), electrons.

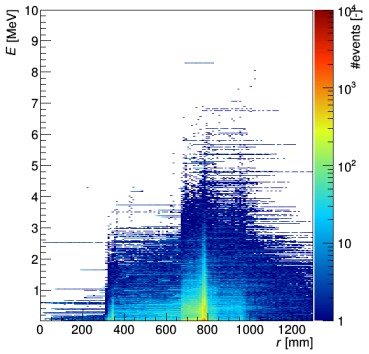

(b) : Production cut 200 µms (≈ 390 keV in steel of vacuum chamber) electrons.

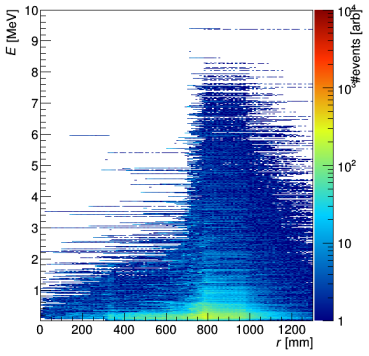

(c) : No production cut (≡ 1 keV in all materials), photons.

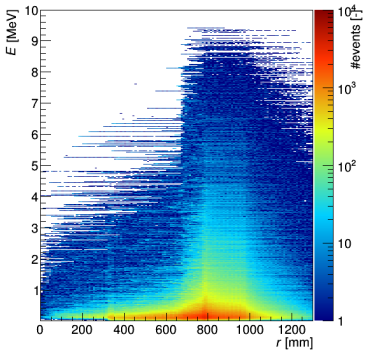

(d) : Production cut 100 µms (≈ 7 keV in steel of vacuum chamber) photons.

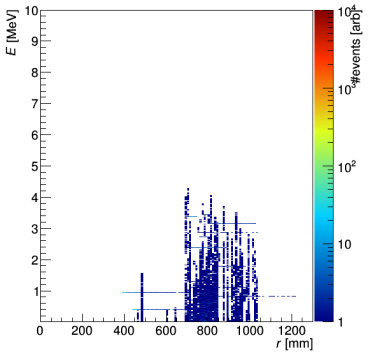

(e) : No production cut (≡ 1 keV in all materials), positrons.

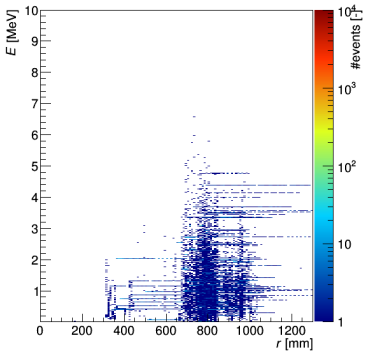

(f) : No production cut (≡ 1 keV in all materials), positrons.

Figure 7: Radial energy profiles of secondary particles. The profile corresponds to the instantaneous energy of all particles dependent on distance r from the middle of the simulated tokamak. Left image represents run without production cut, right is using predefined cut 200 µm for electrons and 100 µm for photons (corresponding to ≈ 390 keV and ≈ 7 keV in steel of vacuum chamber, respectively). Runs were simulated with different number of events (left 100k, right 1.1M).

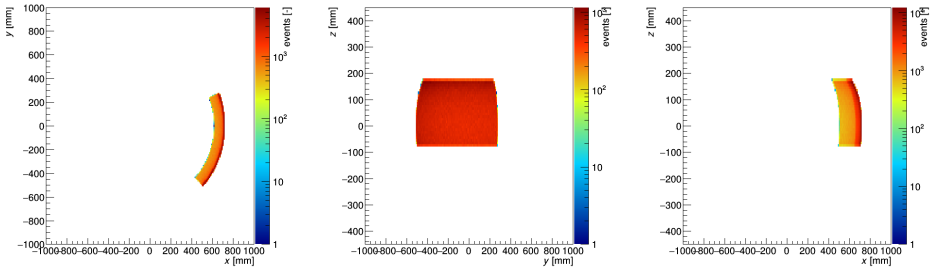

(a) : XY plane. **(b) :** YZ plane. **(c) :** XZ plane.

Figure 8: Spatial distribution of primary particles. Due to the position of Medipix2 detector, toroidal angle φ was set from $-45°$ to $22.5°$ and poloidal angle θ from $-22.5°$ to $60°$.

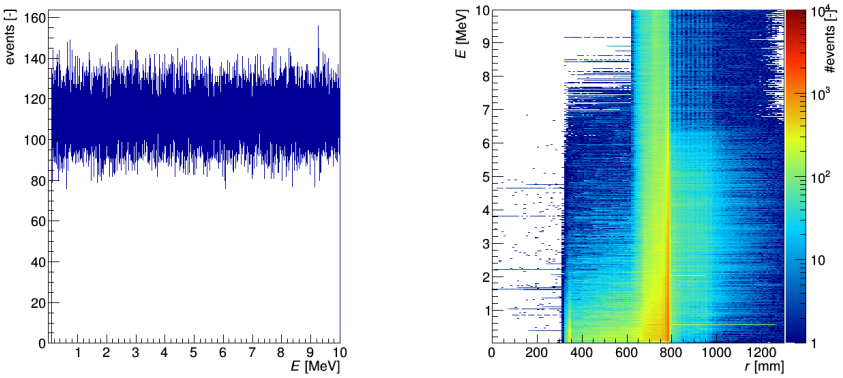

(a) : Energy spectrum. **(b) :** Radial energy profile.

Figure 9: Energy profiles of primary particles. Left image represents initial energy of primary particles, right is integrated radial energy profile.

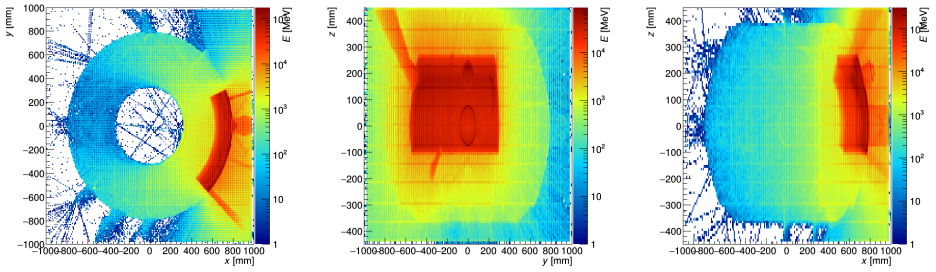

(a) : XY plane, $\alpha = 0\,\text{deg}$. **(b) :** YZ plane, $\alpha = 0\,\text{deg}$. **(c) :** XZ plane, $\alpha = 0\,\text{deg}$.

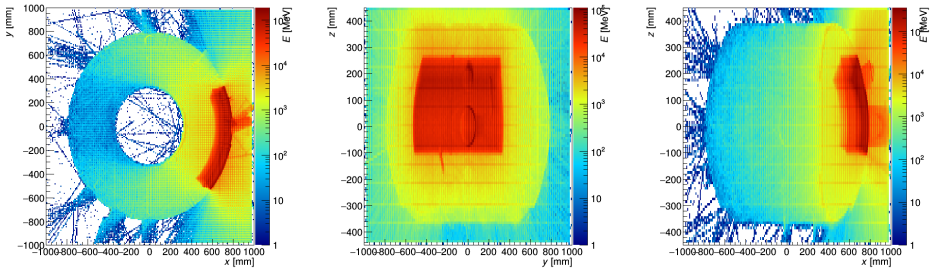

(d) : XY plane, $\alpha = 30\,\text{deg}$. **(e) :** YZ plane, $\alpha = 30\,\text{deg}$. **(f) :** XZ plane, $\alpha = 30\,\text{deg}$.

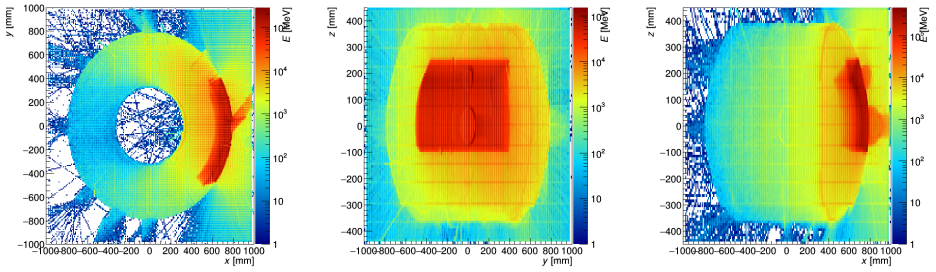

(g) : XY plane, $\alpha = 60\,\text{deg}$. **(h) :** YZ plane, $\alpha = 60\,\text{deg}$. **(i) :** XZ plane, $\alpha = 60\,\text{deg}$.

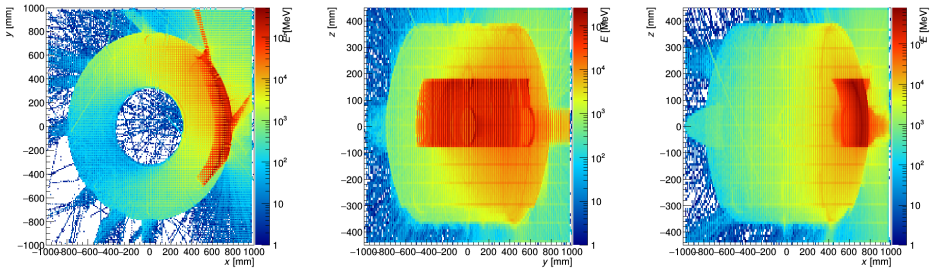

(j) : XY plane, $\alpha = 90\,\text{deg}$. **(k) :** YZ plane, $\alpha = 90\,\text{deg}$. **(l) :** XZ plane, $\alpha = 90\,\text{deg}$.

Figure 10: Integrated tracks of primary particles using their instantaneous energy as a weight. Tracks are visualized for different planes and angles α with respect to the toroidal angle φ.

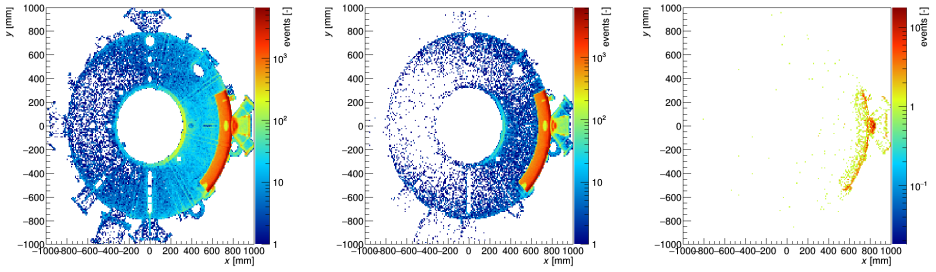

(a) : Electrons, $\alpha = 0\,\text{deg}$. **(b) :** Photons, $\alpha = 0\,\text{deg}$. **(c) :** Positrons, $\alpha = 0\,\text{deg}$.

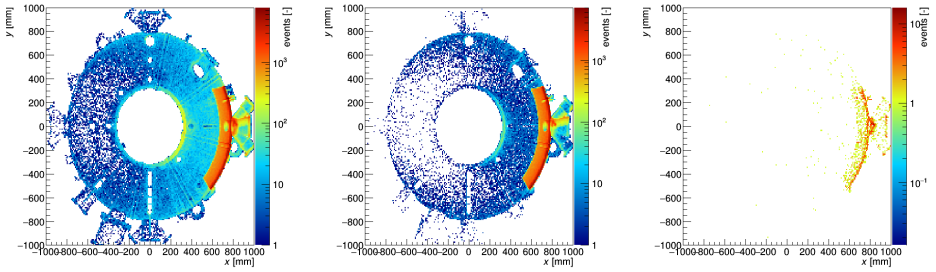

(d) : Electrons, $\alpha = 30\,\text{deg}$. **(e) :** Photons, $\alpha = 30\,\text{deg}$. **(f) :** Positrons, $\alpha = 30\,\text{deg}$.

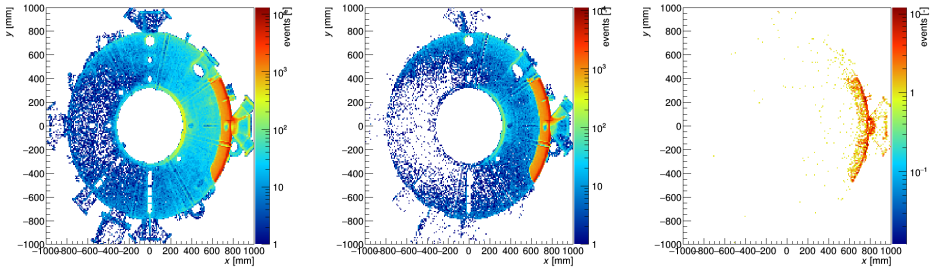

(g) : Electrons, $\alpha = 60\,\text{deg}$. **(h) :** Photons, $\alpha = 60\,\text{deg}$. **(i) :** Positrons, $\alpha = 60\,\text{deg}$.

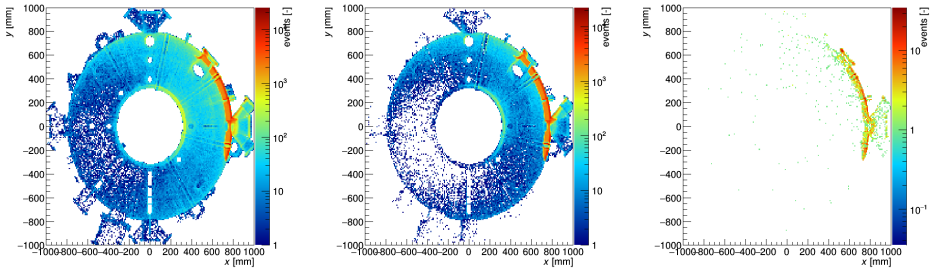

(j) : Electrons, $\alpha = 90\,\text{deg}$. **(k) :** Photons, $\alpha = 90\,\text{deg}$. **(l) :** Positrons, $\alpha = 90\,\text{deg}$.

Figure 11: Spatial distribution of vertices of the secondary particles in XY plane. Visualization made for different secondaries (electrons, photons and positrons) and angles α with respect to the toroidal angle φ.

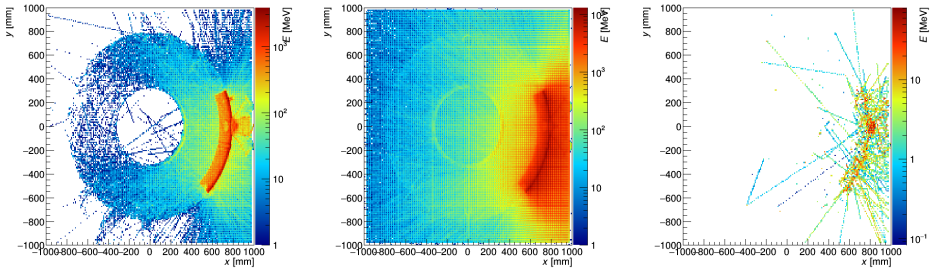

(a) : Electrons, $\alpha = 0\,\text{deg}$. **(b) :** Photons, $\alpha = 0\,\text{deg}$. **(c) :** Positrons, $\alpha = 0\,\text{deg}$.

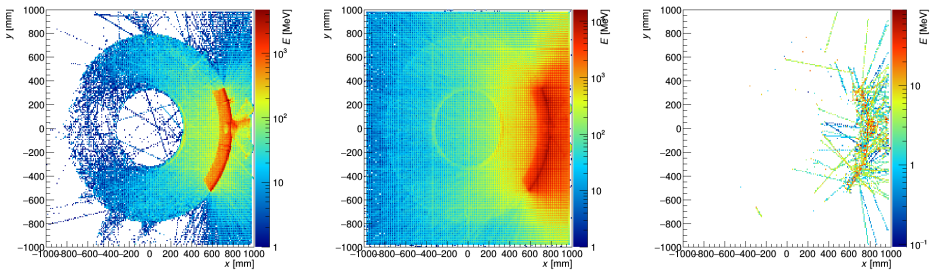

(d) : Electrons, $\alpha = 30\,\text{deg}$. **(e) :** Photons, $\alpha = 30\,\text{deg}$. **(f) :** Positrons, $\alpha = 30\,\text{deg}$.

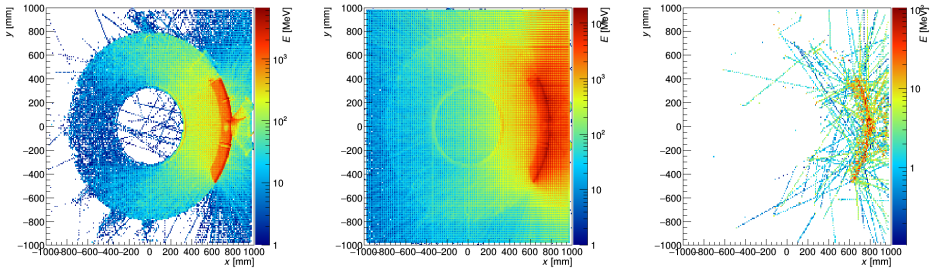

(g) : Electrons, $\alpha = 60\,\text{deg}$. **(h) :** Photons, $\alpha = 60\,\text{deg}$. **(i) :** Positrons, $\alpha = 60\,\text{deg}$.

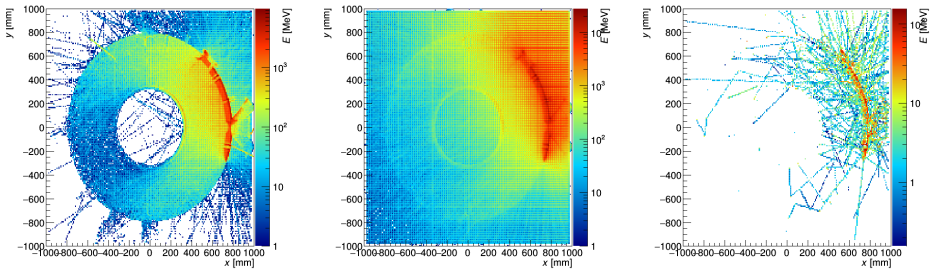

(j) : Electrons, $\alpha = 90\,\text{deg}$. **(k) :** Photons, $\alpha = 90\,\text{deg}$. **(l) :** Positrons, $\alpha = 90\,\text{deg}$.

Figure 12: Integrated tracks of secondary particles using their instantaneous energy as a weight. Tracks are visualized in XY plane for different secondaries (electrons, photons and positrons) and angles α with respect to the toroidal angle φ.

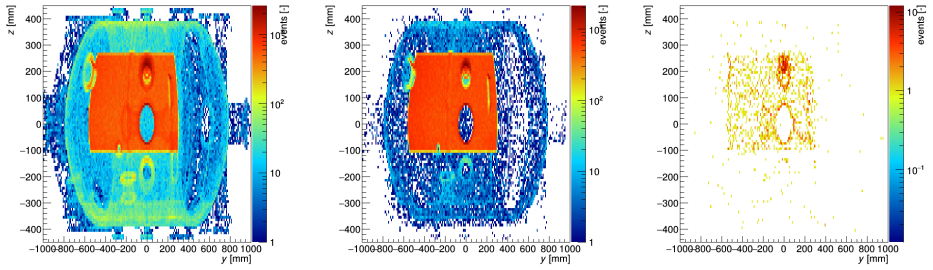

(a) : Electrons, $\alpha = 0\,\text{deg}$. **(b) :** Photons, $\alpha = 0\,\text{deg}$. **(c) :** Positrons, $\alpha = 0\,\text{deg}$.

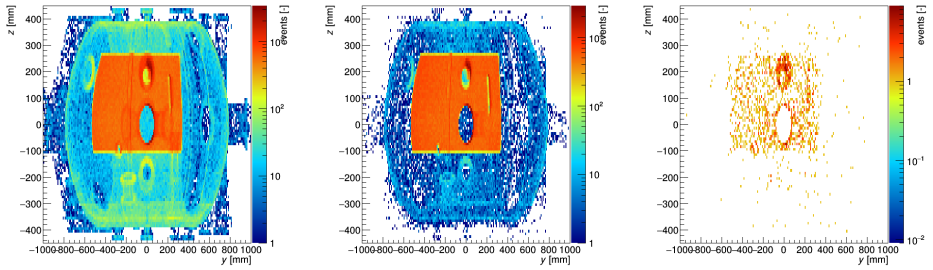

(d) : Electrons, $\alpha = 30\,\text{deg}$. **(e) :** Photons, $\alpha = 30\,\text{deg}$. **(f) :** Positrons, $\alpha = 30\,\text{deg}$.

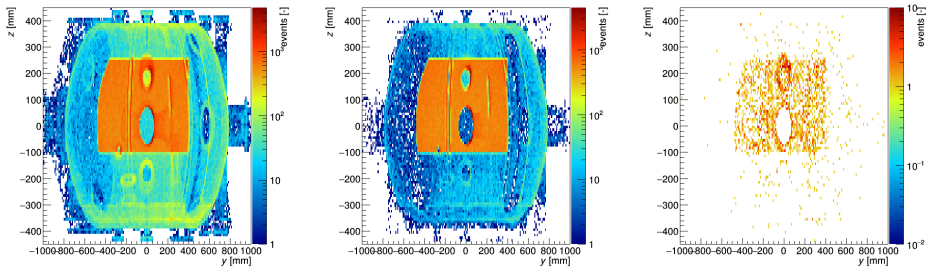

(g) : Electrons, $\alpha = 60\,\text{deg}$. **(h) :** Photons, $\alpha = 60\,\text{deg}$. **(i) :** Positrons, $\alpha = 60\,\text{deg}$.

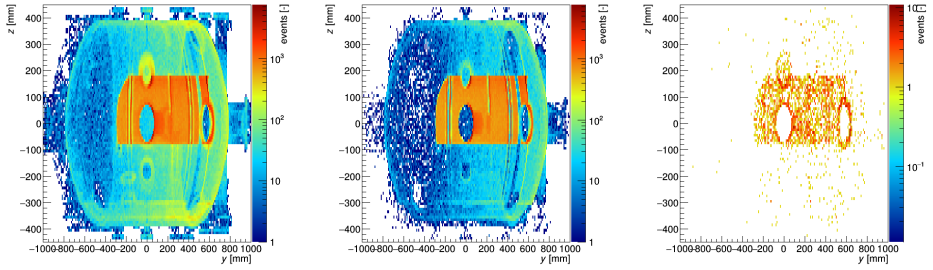

(j) : Electrons, $\alpha = 90\,\text{deg}$. **(k) :** Photons, $\alpha = 90\,\text{deg}$. **(l) :** Positrons, $\alpha = 90\,\text{deg}$.

Figure 13: Spatial distribution of vertices of the secondary particles in YZ plane. Visualization made for different secondaries (electrons, photons and positrons) and angles α with respect to the toroidal angle φ.

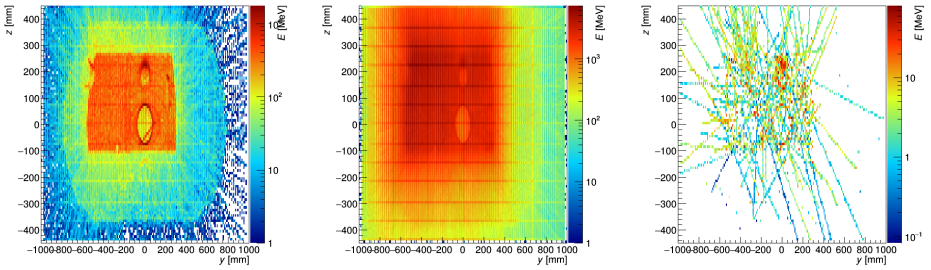

(a) : Electrons, $\alpha = 0\,\text{deg}$. **(b) :** Photons, $\alpha = 0\,\text{deg}$. **(c) :** Positrons, $\alpha = 0\,\text{deg}$.

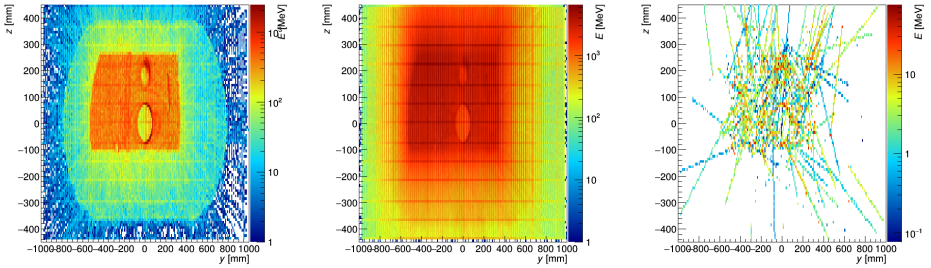

(d) : Electrons, $\alpha = 30\,\text{deg}$. **(e) :** Photons, $\alpha = 30\,\text{deg}$. **(f) :** Positrons, $\alpha = 30\,\text{deg}$.

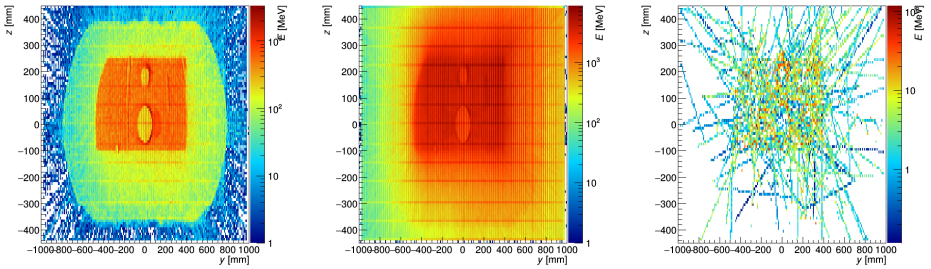

(g) : Electrons, $\alpha = 60\,\text{deg}$. **(h) :** Photons, $\alpha = 60\,\text{deg}$. **(i) :** Positrons, $\alpha = 60\,\text{deg}$.

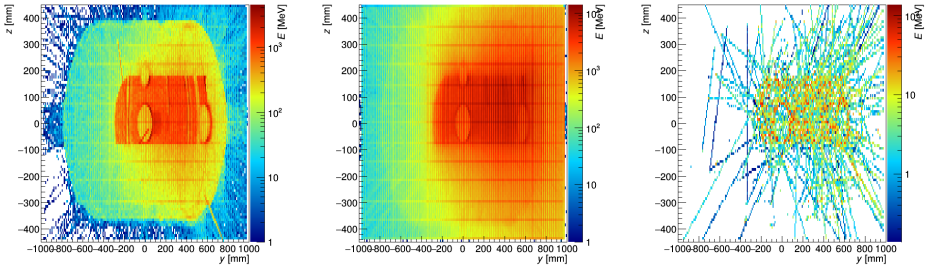

(j) : Electrons, $\alpha = 90\,\text{deg}$. **(k) :** Photons, $\alpha = 90\,\text{deg}$. **(l) :** Positrons, $\alpha = 90\,\text{deg}$.

Figure 14: Integrated tracks of secondary particles using their instantaneous energy as a weight. Tracks are visualized in YZ plane for different secondaries (electrons, photons and positrons) and angles α with respect to the toroidal angle φ.

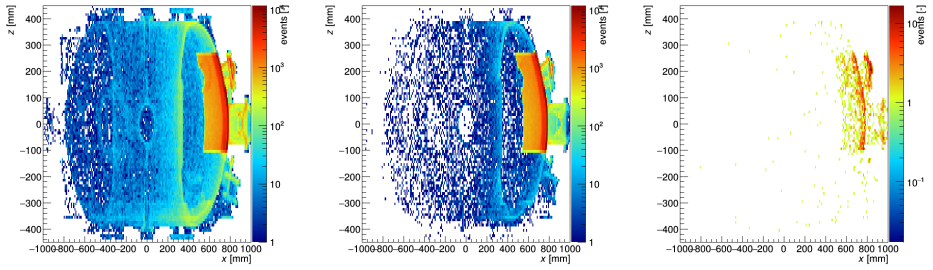

(a) : Electrons, $\alpha = 0\,\text{deg}$. **(b) :** Photons, $\alpha = 0\,\text{deg}$. **(c) :** Positrons, $\alpha = 0\,\text{deg}$.

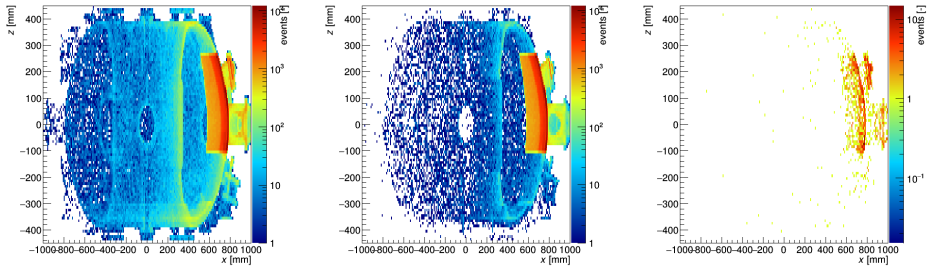

(d) : Electrons, $\alpha = 30\,\text{deg}$. **(e) :** Photons, $\alpha = 30\,\text{deg}$. **(f) :** Positrons, $\alpha = 30\,\text{deg}$.

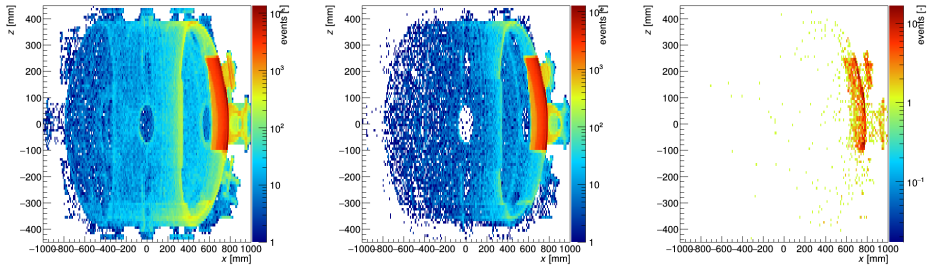

(g) : Electrons, $\alpha = 60\,\text{deg}$. **(h) :** Photons, $\alpha = 60\,\text{deg}$. **(i) :** Positrons, $\alpha = 60\,\text{deg}$.

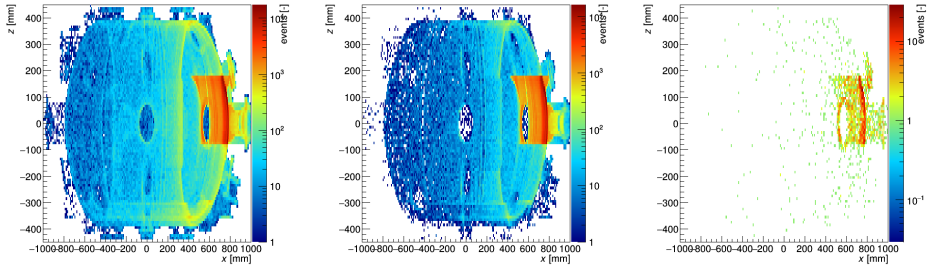

(j) : Electrons, $\alpha = 90\,\text{deg}$. **(k) :** Photons, $\alpha = 90\,\text{deg}$. **(l) :** Positrons, $\alpha = 90\,\text{deg}$.

Figure 15: Spatial distribution of vertices of the secondary particles in XZ plane. Visualization made for different secondaries (electrons, photons and positrons) and angles α with respect to the toroidal angle φ.

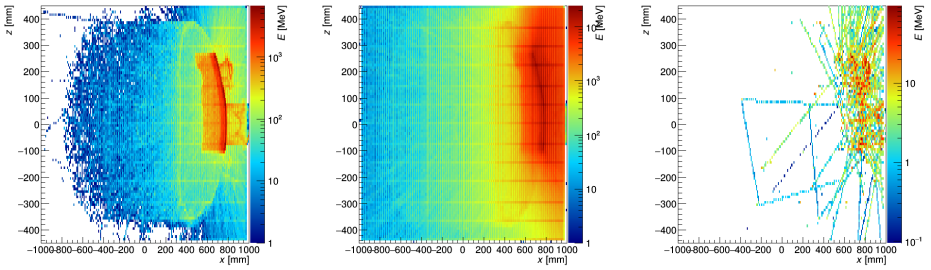

(a) : Electrons, $\alpha = 0\,\text{deg}$. **(b) :** Photons, $\alpha = 0\,\text{deg}$. **(c) :** Positrons, $\alpha = 0\,\text{deg}$.

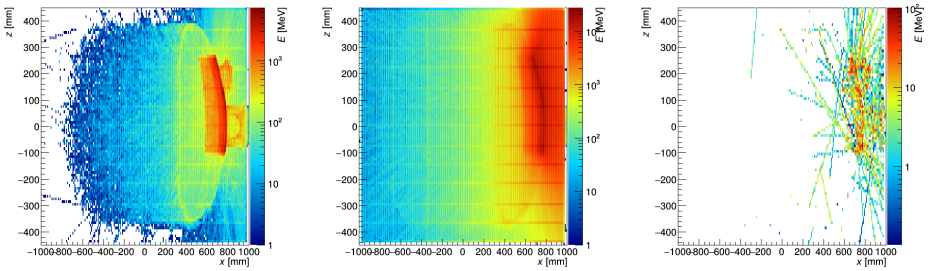

(d) : Electrons, $\alpha = 30\,\text{deg}$. **(e) :** Photons, $\alpha = 30\,\text{deg}$. **(f) :** Positrons, $\alpha = 30\,\text{deg}$.

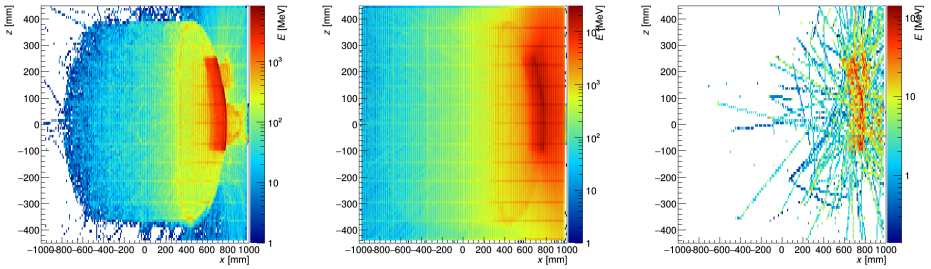

(g) : Electrons, $\alpha = 60\,\text{deg}$. **(h) :** Photons, $\alpha = 60\,\text{deg}$. **(i) :** Positrons, $\alpha = 60\,\text{deg}$.

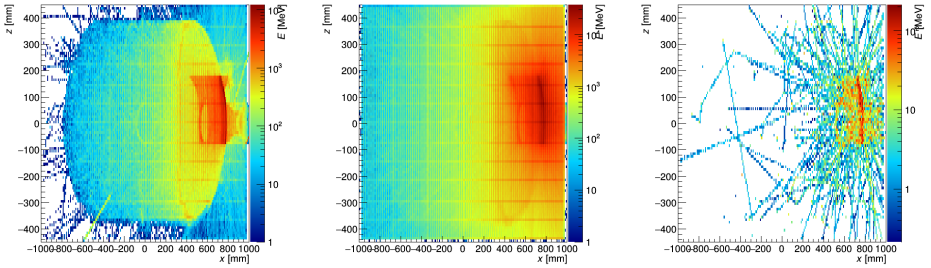

(j) : Electrons, $\alpha = 90\,\text{deg}$. **(k) :** Photons, $\alpha = 90\,\text{deg}$. **(l) :** Positrons, $\alpha = 90\,\text{deg}$.

Figure 16: Integrated tracks of secondary particles using their instantaneous energy as a weight. Tracks are visualized in XZ plane for different secondaries (electrons, photons and positrons) and angles α with respect to the toroidal angle φ.